Delft University of Technology

Investigation of Curle's Dipolar Sources on a Porous Airfoil Interacting with Incoming Turbulence

Zamponi, R.; Satcunanathan, S.; Meinke, M. ; Schröder, W.; Moreau, S.; Schram, C

Important note
To cite this publication, please use the final published version (if applicable).
Please check the document version above.

Investigation of Curle's Dipolar Sources on a Porous Airfoil Interacting with Incoming Turbulence

R. Zamponi*
Delft University of Technology, Delft 2629HS, The Netherlands

S. Satcunanathan[†], M. Meinke[‡], and W. Schröder[§]
RWTH Aachen University, Aachen 52062, Germany

S. Moreau[¶]
Université de Sherbrooke, Sherbrooke J1K 2R1, Canada

C. Schram[‖]
von Karman Institute for Fluid Dynamics, Sint-Genesius-Rode 1640, Belgium

Integrating porous materials into the structure of an airfoil constitutes a promising passive strategy for mitigating the noise from turbulence-body interactions that has been extensively explored in the past few decades. When a compact permeable body is considered in the aeroacoustic analogy derived by Curle to predict this noise source, a dipole associated with the nonzero unsteady Reynolds stresses appears on the surface in addition to the dipole linked to the pressure fluctuations. Nevertheless, the relative contribution of this source on the far-field noise radiated by a porous wing profile has not been clarified yet. The purpose of the current research work is twofold. On the one hand, it investigates the impact of porosity on the surface-pressure fluctuations of a thick airfoil immersed in the wake of an upstream circular rod at a Mach number of 0.09. On the other hand, it quantifies the relevance of the Reynolds-stresses term on the surface as a sound-generation mechanism. Results from large-eddy simulations show that the porous treatment of the wing profile yields an attenuation of the unsteady-pressure peak, which is localized in the low-frequency range of the spectrum and is induced by the milder distortion of the incoming vortices. However, porosity is ineffective in breaking the spanwise coherence or in-phase behavior of the surface-pressure fluctuations at the vortex-shedding frequency. The Reynolds-stresses term is found to be considerable in the stagnation region of the airfoil, where the transpiration velocity is larger, and partly correlated with the unsteady surface pressure. This results in a nonnegligible contribution of this term to the far-field acoustic pressure emitted by the porous wing profile for observation angles near the stagnation streamline. The conclusions drawn in the present study eventually provide valuable insight into the design of innovative and efficient passive strategies to mitigate surface-turbulence interaction noise in industrial applications.

I. Introduction

THE aerodynamic noise generated by the impingement of a turbulent flow on the surface of a wing represents a topic of active research that is related to numerous industrial applications. For instance, the noise due to the periodic interaction of the fan wakes with the outlet guiding vanes (OGV) in modern turbofan engines [1] is receiving increasing attention due to the ever-larger bypass ratios adopted in their design, which, in turn, result in a decreased axial distance between fan and OGV and enhanced noise emissions [2]. Consequently, a significant effort has been put into mitigating

---

*Postdoctoral Researcher, Department of Aerodynamics, Wind Energy, Flight Performance and Propulsion, r.zamponi@tudelft.nl, AIAA Member
†Research Scientist, Institute of Aerodynamics, s.satcunanathan@aia.rwth-aachen.de
‡Senior Scientist, Institute of Aerodynamics, m.meinke@aia.rwth-aachen.de
§Professor, Institute of Aerodynamics, office@aia.rwth-aachen.de, AIAA member
¶Professor, Département de Génie Mécanique, stephane.moreau@usherbrooke.ca, AIAA member
‖Professor, Environmental and Applied Fluid Dynamics Department & Aeronautics and Aerospace Department, christophe.schram@vki.ac.be, AIAA member

this source of noise, and one of the promising passive solutions proposed so far is to integrate porous materials into the structure of the wing or blade profile [3].

From a physical perspective, the turbulent eddies interacting with the leading edge of an airfoil are subjected to a rapid distortion responsible for scattering part of their kinetic energy into sound [4], which is usually referred to as turbulence-interaction or leading-edge noise. A popular predictive method for the noise produced by this mechanism is based on the concept of aeroacoustic analogies. Lighthill [5] first demonstrated that the mechanisms accountable for the aerodynamic sound emitted by a turbulent flow can be represented, from the listener's point of view, by equivalent sources placed in a quiescent uniform medium. Such an approach has proved to be effective especially for low Mach number applications. Lighthill's analogy was subsequently extended by Curle [6], who accounted for the presence of a body immersed in the flow and described the additional equivalent sources that arise due to turbulence-surface interactions as acoustic dipoles. These are associated with the reaction force that the body exerts on the surrounding fluid and are typically dominant at low Mach numbers. The topic of the present work is to investigate the influence of porous materials on the generation and propagation of such dipolar sources.

The idea of applying porosity as a passive noise-attenuation strategy has been considerably explored among the aeroacoustic community in the last three decades. The beneficial effects of the porous treatment of an airfoil were first proved by Lee [7], who showed that the integration of a permeable leading-edge insert into a helicopter blade resulted in a far-field noise reduction of up to 30 % due to the suppression of the unsteady pressure on the blade surface. Geyer *et al.* [8, 9] investigated the influence of the porous properties on the turbulence-interaction noise mitigation and concluded that higher values of static permeability yield more substantial attenuation at low frequencies but also increase at high frequencies due to the augmented surface roughness. The experimental dataset produced in that study was then exploited by Sarradj and Geyer [10] using symbolic-regression tools to analyze the sensitivity of the different flow and material parameters on leading-edge noise. The results highlighted a dependency on the square of the turbulence intensity and from the fifth to the sixth power of the incoming mean-flow velocity. Furthermore, the ratio of the integral length scale of turbulence to the characteristic length of the porous structure, which is defined as the square root of the static permeability of the medium, was found to affect the far-field acoustic spectrum significantly.

When the full chordwise extent of the airfoil is made permeable, a noticeable deterioration of the aerodynamic performance is expected, resulting in a decrease in the lift force and an increase in the drag force. The former is related to the pressure communication between the two sides of the airfoil through the pores of the material, whereas the latter is mainly linked to the higher surface roughness. The penalization is more crucial at higher angles of incidence [8, 11–13]. A possible technological solution for counteracting the above-mentioned effects is to limit the region of the wing profile where the flow can permeate to the leading edge [13–15] or integrate the porous medium in a rigid permeable exoskeleton including a solid centerplane to avoid crossflow between the pressure and suction sides [16–18]. These options allow finding a trade-off among turbulence-interaction noise reduction, aerodynamic-performance conservation, and structural-integrity preservation.

More recently, novel concepts for designing porous airfoils based on nonuniform distributions of porosity have been proposed. Paruchuri *et al.* [19], Palleja-Cabre *et al.* [20], and Priddin *et al.* [21] investigated the leading-edge noise reduction achieved by flat plates with different extents of porous inserts and showed that a single row of holes located downstream of the stagnation point results in significant mitigation at low frequencies without increasing the noise emissions at high frequencies. Ayton *et al.* [22] found that smoothly varying chordwise porosity on a perforated flat plate can be beneficial for reducing trailing-edge noise thanks to the more significant destructive interference of the back-scattered field generated by the impermeable leading edge [23, 24]. Moreover, Ayton *et al.* [25] observed that a spanwise-varying distribution of perforations on a flat plate could theoretically yield lower noise levels if compared with uniform porosity with a mechanism similar to that induced by leading-edge serrations. These studies demonstrate that the research on innovative porous materials is currently active, and there is room for further optimization of the performance of such a passive noise-reduction strategy.

The present work represents the continuation of some research previously initiated by the authors. Specifically, Zamponi *et al.* [26] designed a porous airfoil that integrates melamine foam into a permeable hard-plastic exoskeleton shaped as a NACA-0024 profile. A centerplane prevents the communication between the two sides of the model, while the surface is coated with a metallic wire mesh that guarantees a surface roughness with the desired quality. The airfoil was placed in the wake generated by an upstream circular cylinder and compared with a solid baseline, highlighting a leading-edge noise decrease of up to 2 dB at low frequencies. In addition, large-eddy simulations (LES) for this experimental setup were carried out by Satcunanathan *et al.* [27] to shed additional light upon the flow-field alterations caused by porosity. Both measurements and numerical computations were further analyzed by Zamponi *et al.* [28, 29], who identified the milder distortion experienced by the largest turbulent eddies as one of the prevalent noise-mitigation

mechanisms related to the porous treatment of the wing profile. This link was subsequently confirmed by Tamaro *et al.* [30] with particle image velocimetry and acoustic far-field measurements. Furthermore, a model based on the rapid distortion theory (RDT) [31] was proposed by Zamponi *et al.* [32] to predict the changes in the turbulent velocity experienced by a porous body that interacts with prescribed incoming turbulence. Such a semi-analytic method could lay the foundation for developing novel noise-prediction tools for porous airfoils.

While the studies outlined above provide some insight on the attenuation of the distortion of incoming turbulence, the impact of porosity on Curle's dipolar sources has not been addressed. Moreover, the integral solution of Lighthill/Curle's analogy assumes no-slip and nonpenetration boundary conditions at the surface of the body surrounded by turbulence. This assumption is no longer valid when the surface is permeable, so additional equivalent-source terms appear in the derivation. A better understanding of how these are affected would be instrumental in designing more effective noise-reduction techniques and constitutes the objective pursued in the present research. The information on the flow field extracted from the LES data produced and validated in the previous works is considered here. The results of this investigation will eventually provide useful insight into the design of innovative and more effective porous treatments.

The paper is structured as follows. A recap of the derivations of Curle's analogy is reported in Section II. Section III discusses the computational methodology and gives a brief description of the model equations for the porous media and the turbulent-flow prediction. In Section IV, the numerical setup, flow conditions, and data processing settings are described. Section V presents the achieved results, addressing the role of porosity on Curle's dipolar sources on the airfoil surface. Finally, conclusions are drawn in Section VI.

II. Theory: Curle's analogy for a porous body

Upon definition of a thermodynamic reference state indicated by the density ρ_0 and pressure p_0 that refer to a uniform medium at rest, the propagation of density perturbations $\rho' = \rho - \rho_0$ at the speed of sound $c_0 = \sqrt{(\partial p / \partial \rho)_s}$, s being the entropy, in a homogeneous acoustic medium is described by Lighthill's analogy [5] as

$$\frac{\partial^2 \rho'}{\partial t^2} - c_0^2 \frac{\partial^2 \rho'}{\partial x_i^2} = \frac{\partial^2 T_{ij}}{\partial x_i \partial x_j}, \tag{1}$$

where $T_{ij} = \rho u_i u_j - \tau_{ij} + (p' - c_0^2 \rho') \, \delta_{ij}$ is denoted as Lighthill's stress tensor [5], which accounts for the sound produced by Reynolds stresses $\rho u_i u_j$, $\boldsymbol{u}$ being the flow velocity, viscous stresses τ_{ij}, and nonisentropic processes. Here, δ is the Dirac delta function. For high Reynolds numbers, the contribution of the viscous forces can be neglected and with the assumption of incompressible and isentropic flow, Lighthill's stress tensor can be approximated as $T_{ij} \approx \rho_0 u_i u_j$.

In the presence of a stationary surface S in the control domain V, the solution of Eq. (1) using the Green's function approach [33] can be expressed for a listener located at position $\boldsymbol{x}$ in space at time t and a source placed at position $\boldsymbol{y}$ in space at emission time τ by

$$c_0^2 \rho'(\boldsymbol{x}, t) = \int_{-\infty}^{t} \iiint_V \frac{\partial^2 T_{ij}}{\partial y_i \partial y_j} G \, \mathrm{d}V \, \mathrm{d}\tau + c_0^2 \int_{-\infty}^{t} \iint_S \left(\rho' \frac{\partial G}{\partial y_i} - G \frac{\partial \rho'}{\partial y_i} \right) n_i \, \mathrm{d}S \, \mathrm{d}\tau, \tag{2}$$

where $\boldsymbol{n}$ is the outward-pointing normal on S and G is the Green's function [34]. The first term in the right-hand side of the equation indicates the incident acoustic field, whereas the second one represents the sound radiated by the vibration of the surface. The incident-field integral can be reformulated by performing an integration by parts, and the partial derivatives can be moved from the source to the Green's function. Using the divergence theorem and imposing the momentum conservation law [33], Eq. (2) becomes

$$p^*(\boldsymbol{x}, t) = \int_{-\infty}^{t} \iiint_V \frac{\partial^2 G}{\partial y_i \partial y_j} T_{ij} \, \mathrm{d}V \, \mathrm{d}\tau + c_0^2 \int_{-\infty}^{t} \iint_S \left[G \frac{\partial \rho u_i}{\partial \tau} + (p' \delta_{ij} + \rho u_i u_j) \frac{\partial G}{\partial y_i} \right] n_i \, \mathrm{d}S \, \mathrm{d}\tau \tag{3}$$

where $p^* \equiv c_0^2 \rho'$ denotes the acoustic pressure at the listener position. The viscous stresses have been neglected with regard to the pressure fluctuations and Reynolds stresses in the last integral, owing to the assumed large Reynolds number. If the body is impermeable, the velocity u_i on the surface is zero and the terms $\partial \rho u_i / \partial \tau$ and $\rho u_i u_j$ in the surface integral vanish. Conversely, for a porous surface, the flow penetration within the inner volume of the body is permitted, and these two terms have to be retained.

3

Subsequently, the application of the free-field Green's function

$$G_0(\boldsymbol{x}, t | \boldsymbol{y}, \tau) = \frac{\delta(t - \tau - ||\boldsymbol{x} - \boldsymbol{y}||/c_0)}{4\pi \, ||\boldsymbol{x} - \boldsymbol{y}||} \tag{4}$$

makes it possible to carry out the time integrals in Eq. (3) [6], yielding

$$p^*(\boldsymbol{x}, t) = \frac{\partial^2}{\partial x_{\mathrm{i}} \partial x_{\mathrm{j}}} \iiint_V \left[\frac{T_{\mathrm{ij}}}{4\pi \, ||\boldsymbol{x} - \boldsymbol{y}||} \right]_{t=\hat{\tau}} \mathrm{d}V$$
$$- \frac{\partial}{\partial x_{\mathrm{i}}} \iint_S \left[\frac{p'\delta_{\mathrm{ij}} + \rho u_{\mathrm{i}} u_{\mathrm{j}}}{4\pi \, ||\boldsymbol{x} - \boldsymbol{y}||} \right]_{t=\hat{\tau}} n_{\mathrm{j}} \, \mathrm{d}S + \iint_S \left[\frac{\partial \rho u_{\mathrm{j}}}{\partial \tau} \frac{1}{4\pi \, ||\boldsymbol{x} - \boldsymbol{y}||} \right]_{t=\hat{\tau}} n_{\mathrm{j}} \, \mathrm{d}S, \quad (5)$$

where $\hat{\tau} = t - ||\boldsymbol{x} - \boldsymbol{y}||/c_0$ is the retarded time at which the source terms are evaluated. Furthermore, if the body is assumed to be acoustically compact, i.e., the size of the source region is small compared with the acoustic wavelength, the variation of $\hat{\tau}$ over the surface can be neglected and the square brackets can be moved out of the integral. Additionally, in the geometric far-field, namely at a distance much greater than the characteristic dimension of the body, the term $4\pi \, ||\boldsymbol{x} - \boldsymbol{y}||$ can be approximated to $4\pi \, r$, r being the averaged distance between the source region and listener.

The outcome of the analysis is that multiple terms contribute to the radiated sound when a permeable or a rigid-permeable surface is immersed in a turbulent flow. The first volume integral in the right-hand side of Eq. (5) is the usual quadrupolar term of Curle's integral solution. By using the relation [33]

$$\frac{\partial f(\hat{\tau})}{\partial x_{\mathrm{i}}} = \left[\frac{\partial f(\tau)}{\partial \tau} \right]_{\tau=\hat{\tau}} \frac{\partial \hat{\tau}}{\partial x_{\mathrm{i}}} = \frac{-(x_{\mathrm{i}} - y_{\mathrm{i}})}{||\boldsymbol{x} - \boldsymbol{y}||c_0} \left[\frac{\partial f(\tau)}{\partial \tau} \right]_{\tau=\hat{\tau}} \tag{6}$$

and dropping the terms of order $1/r^2$ and $1/r^3$ that can be considered negligible in the geometric far-field, the quadrupolar term becomes

$$p^*_{\mathrm{quadrupole}}(\boldsymbol{x}, t) \approx \frac{x_{\mathrm{i}} x_{\mathrm{j}}}{4\pi \, c_0^2 r^3} \left[\iiint_V \frac{\partial^2 T_{\mathrm{ij}}}{\partial \tau^2} \, \mathrm{d}V \right]_{\tau=\hat{\tau}}. \tag{7}$$

The first surface integral in the right-hand side of Eq. (5) is the dipolar term, which accounts for the surface loading and typically dominates over the quadrupolar one for low Mach number applications and acoustically compact source regions. From Eq. (6) and considering the far-field approximation, it follows that

$$p^*_{\mathrm{dipole}}(\boldsymbol{x}, t) \approx \frac{x_{\mathrm{i}}}{4\pi \, c_0 r^2} \left[\iint_S \frac{\partial \left(p'\delta_{\mathrm{ij}} + \rho u_{\mathrm{i}} u_{\mathrm{j}} \right)}{\partial \tau} n_{\mathrm{j}} \, \mathrm{d}S \right]_{\tau=\hat{\tau}}. \tag{8}$$

Equation (8) states that the distribution of dipoles representing fluctuating forces acting on the fluid from the porous body is produced by two components, one linked to the surface-pressure fluctuations, denoted as *unsteady-pressure term*, and the other one to the variation of Reynolds stresses on the surface, indicated as *Reynolds-stresses term*. For an impermeable body, only the former is nonzero, whereas the latter appears solely when the airflow can penetrate the inner volume of the body, i.e., with a porous material. In Section V, the contribution to the far-field acoustic pressure provided by these terms will be evaluated separately.

Finally, the second surface integral in the right-hand side of Eq. (5) is the monopolar term, which is related to the rate of mass flux across the body surface and can be expressed as

$$p^*_{\mathrm{monopole}}(\boldsymbol{x}, t) \approx \frac{1}{4\pi \, r} \left[\iint_S \frac{\partial \rho u_{\mathrm{j}}}{\partial \tau} n_{\mathrm{j}} \, \mathrm{d}S \right]_{\tau=\hat{\tau}}. \tag{9}$$

By exploiting the reciprocity principle according to which $\partial/\partial \tau = -\partial/\partial t$, the time derivative can be moved out of the surface integral, and this term is null by the conservation of mass. However, it is worth pointing out that when the assumption of acoustic compactness is not verified, i.e., the variation of retarded time over the surface is not negligible anymore, the monopolar term may contribute to the overall sound produced by a porous body immersed in a turbulent flow. This equivalent source would have a dipolar efficiency at leading order due to the destructive interference between the surface patches where the flow is entering and leaving the body. Studying this noise source will undoubtedly be a topic for future work.

4

III. Computational methodology

As introduced in Section I, the turbulent-flow field is predicted using an LES based on the compressible Navier-Stokes equations. These equations are equally valid inside the porous material and can be employed to fully resolve the flow through the porous microstructures, though being computationally challenging for various reasons. On the one hand, this requires the complex pore morphology to be available, e.g., with a computerized tomography scan, which is often not the case. On the other hand, the requirement on the grid resolution would be severe due to the tiny pore structures being typically smaller than the smallest length scale of the turbulence.

Often, only the integral effects or the flow alterations in the outer region by a porous treatment are of interest. A well-established approach is to neglect the microscale introduced by the pores of the material by the method of volume averaging [35, 36]. This procedure replaces the distinct fluid and solid regions in the porous material by a locally homogeneous medium with continuously varying field variables. These are then governed by the volume-averaged Navier-Stokes equations (VANS) augmented by closure terms, which emerge from the spatial filtering process and account for subgrid effects. For more details, the reader is referred to Satcunanathan *et al.* [27].

In the subsequent brief consideration, let Ω be the total simulation domain, $\Omega_f = \{ \boldsymbol{x} \in \Omega \mid \varphi(\boldsymbol{x}) = 1 \}$ the fluid region, $\Omega_p = \{ \boldsymbol{x} \in \Omega \mid \varphi(\boldsymbol{x}) < 1 \}$ the porous region with $\Omega_g \cap \Omega_p = \emptyset$, and $\Gamma = \partial \Omega_f \cap \Omega_p$ the fluid-porous interface. The porosity φ is the volume ratio of the open pores to the total volume of the porous material, and is equal to 1 in the free fluid. Using the symbol $\langle \ \rangle$ to denote the intrinsic average and $\langle \ \rangle_F$ the Favre average, the conservation of mass, momentum, and energy in nondimensional integral form formulated for an arbitrary control volume V reads

$$\frac{\mathrm{d}}{\mathrm{d}t} \int_{V \in \Omega} \boldsymbol{Q} \, \mathrm{d}V + \oint_{\partial V \in \Omega} \left(\boldsymbol{H}^{\mathrm{inv}} - \boldsymbol{H}^{\mathrm{vis}} \right) \cdot \boldsymbol{n} \, \mathrm{d}S + \int_{V \in \Omega} \left(\frac{1}{\varphi} \boldsymbol{H}^{\mathrm{inv}} \cdot \nabla \varphi + \boldsymbol{S} \right) \mathrm{d}V = 0, \tag{10}$$

where $\boldsymbol{Q} = [\langle \rho \rangle, \langle \rho \rangle \langle \boldsymbol{u} \rangle_F, \langle \rho \rangle \langle E \rangle_F]^T$ is the vector of spatially-averaged conservative variables. The inviscid and viscous flux tensors are given by

$$\boldsymbol{H}^{\mathrm{inv}} - \boldsymbol{H}^{\mathrm{vis}} = \begin{bmatrix} \langle \rho \rangle \langle \boldsymbol{u} \rangle_F \\ \langle \rho \rangle \langle \boldsymbol{u} \rangle_F \otimes \langle \boldsymbol{u} \rangle_F + \langle p \rangle \boldsymbol{I} \\ \langle \rho \rangle \langle E \rangle_F \langle \boldsymbol{u} \rangle_F + \langle p \rangle \langle \boldsymbol{u} \rangle_F \end{bmatrix} - \frac{1}{Re} \begin{bmatrix} 0 \\ \langle \boldsymbol{\tau} \rangle_F \\ \langle \boldsymbol{\tau} \rangle_F \cdot \langle \boldsymbol{u} \rangle_F + \frac{1}{Pr} \langle \boldsymbol{q} \rangle \end{bmatrix}. \tag{11}$$

The quantities E, $\boldsymbol{q}$, $\boldsymbol{I}$, Re, and Pr denote the total energy, heat-flux vector, unit tensor, Reynolds number, and Prandtl number, respectively. The first two integrals in Eq. (10) are formally identical to the equations solved in a monotone integrated LES (MILES) context for $\varphi = 1$, where no explicit modeling of the subgrid scale is used. The first term in the last integral is the contribution of the inviscid flux vector at the fluid-porous interface $\boldsymbol{H}^{int} = \boldsymbol{H}^{\mathrm{inv}} - \langle p \rangle \boldsymbol{I}$. The surface-filter term

$$\boldsymbol{S} = \begin{cases} [0, \boldsymbol{F}/\varphi, 0]^T, & \boldsymbol{x} \in \Omega_p \\ \boldsymbol{0}^T, & \boldsymbol{x} \in \Omega_f \end{cases} \tag{12}$$

contains the porous-drag vector $\boldsymbol{F}$ that is closed through the Darcy-Forchheimer model [37, 38], expressed for a homogeneous and isotropic porous medium as

$$\boldsymbol{F} = \underbrace{\frac{1}{Re_k \sqrt{Da}} \varphi \mu \langle \boldsymbol{u} \rangle_F}_{\text{Darcy}} + \underbrace{\frac{1}{\sqrt{Da}} \varphi^2 c_F \langle \rho \rangle |\langle \boldsymbol{u} \rangle_F| \langle \boldsymbol{u} \rangle_F}_{\text{Forchheimer}}. \tag{13}$$

The permeability Reynolds number, $Re_k = Re \sqrt{Da}$, is computed with $d_p \sim \sqrt{k}$ as the length scale, which is a measure for the effective pore diameter, while the Darcy number, Da, is defined as $Da = k/L^2$, L being a reference length. The Darcy-Forchheimer model in Eq. (13), together with Eq. (10), characterizes the porous medium in terms of the porosity, φ, static permeability, k, and Forchheimer coefficient, c_F, and assumes the porous frame to be rigid, neglecting coupling effects due to elasticity as well as thermal effects. The equations are solved by a finite-volume method, which has been discretised in space by an advective upstream splitting method (AUSM) for the inviscid fluxes and a centered discretisation of the viscous fluxes. The semi-discretised equations are advanced in time by a five-stage explicit Runge-Kutta scheme. The overall scheme is second-order accurate in space and time, while the LES is based on the MILES ansatz. The equations are discretised on a locally refined, unstructured, Cartesian mesh with a fully conservative cut-cell approach for the wall boundaries [39].

Equation (10) is valid in the pure fluid and pure porous regions, but assumptions made during the derivation are violated across the fluid-porous interface Γ. Additionally, the sudden change of φ across Γ makes the equations stiff. It can be shown that the arising Dirac-shaped source terms can be equally replaced by jumps of the flow variables across an idealized sharp immersed fluid-porous interface on a noninterface fitted Cartesian mesh. In such a fluid-porous cut cell, the volume-weighted average of the state vector $\boldsymbol{Q} = \varphi\,\boldsymbol{Q}_f + (1 - \varphi)\,\boldsymbol{Q}_p$ is integrated in time, preventing the emergence of small cells, which may pose stringent timestep constraints for hyperbolic solvers. In this case, the flow variables on the porous surface correspond to $\boldsymbol{Q}_f$ of the respective cut cell. For a more detailed description of the method, the reader is referred to [27].

IV. Computational setup
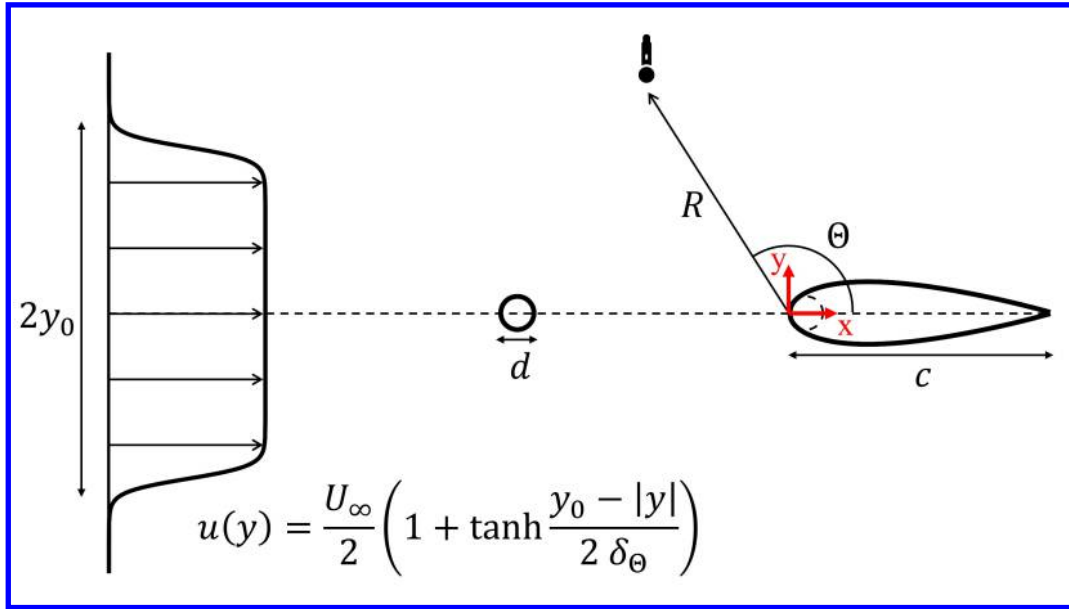
(a)
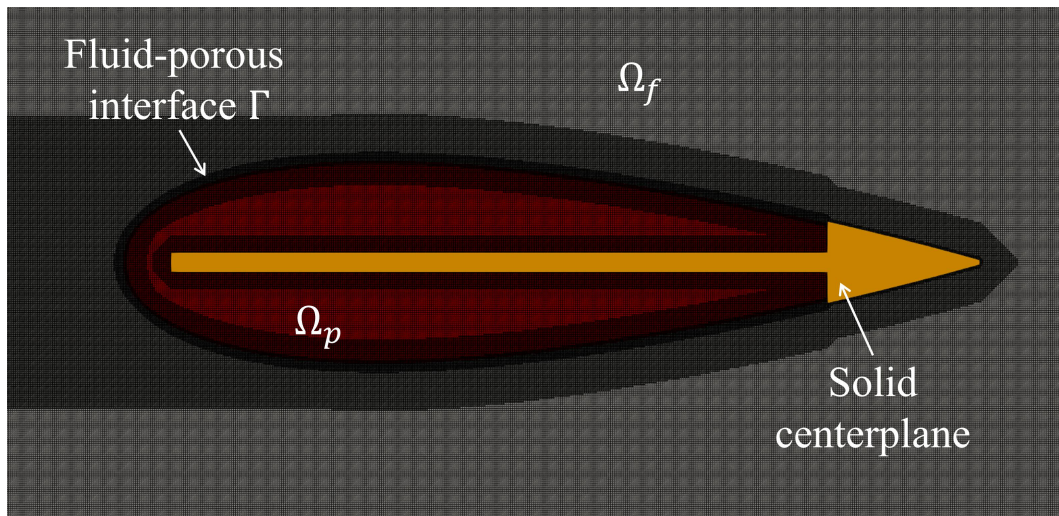
(b)

Fig. 1   (a) 2D sketch of the rod-airfoil configuration. (b) Close-up view of a locally refined Cartesian grid of the porous airfoil. The part of the wing profile made of melamine foam is indicated in red.

The observations and outcome of the theoretical analysis in Section II will be applied to the existing numerical

6

simulation data of a rod-airfoil configuration being already the subject of previous leading-edge noise investigations [27, 28].

A. Rod-airfoil configuration

In the rod-airfoil arrangement, first conceived by Jacob *et al.* [40] as an aeroacoustic benchmark problem, the wing profile undergoes a broadband perturbation dominated by a specific shedding frequency, similar to several aeronautical applications [41]. In the discussion below, all lengths are given as multiple of the cylindrical rod diameter $d = 0.02$ m, which is located $8.2\,d$ upstream of a two-dimensional NACA-0024 profile with $c = 7.85\,d$ chord length and a leading-edge radius of $r_{LE} = 0.5\,d$ at 0° angle of attack. The rather thick airfoil will cause a considerable displacement and distortion of the mean flow, the implications of which have been formerly analyzed in [28].

In Fig. 1a, the overall arrangement is symmetrical with respect to the streamwise direction, and the coordinate system used in the present study is defined as follows: the x-axis is aligned with the streamwise direction, the y-axis is aligned with the upwash direction, and the z-axis is aligned in the spanwise direction to form a right-handed coordinate system with the origin at the leading edge of the wing profile. The rod and airfoil are placed in the potential core of a plane jet of Mach number $M = 0.09$ and width $7.5\,d$. At the inlet, a tangent hyperbolic velocity profile with super-imposed synthetic eddies [42] generating a 1 % turbulence intensity is prescribed to simulate realistic atmospheric or wind tunnel disturbances of the incident flow. The jet shear-layer thickness is initialized to $\delta_\Theta/d = 0.04$. To avoid the emergence of large Kelvin-Helmholtz type roll-ups that might contaminate the flow around the airfoil, a shear layer break-up was induced using the jet shear-layer forcing proposed by Bogey and Bailly [43].

The Reynolds number based on the rod diameter and on the wing-profile chord are $Re_d = 4.0 \times 10^4$ and $Re_c = 3.14 \times 10^5$, which corresponds to a free-stream flow velocity of $30\,\mathrm{m\,s^{-1}}$. Under these conditions, a turbulent wake with embedded shed vortices will impinge on the airfoil leading edge.

B. Solid and porous-airfoil models

Simulations of two configurations, differing in the material of the NACA-0024 profile, have been conducted. The first is a classical solid airfoil where the no-slip boundary condition is satisfied on the surface. The second is a wing profile whose bulk volume is assumed to be porous, as indicated in Fig. 1b. An impermeable centerplane preventing the crossflow between the upper and lower sides of the airfoil (see Section I) extends from one leading-edge radius downstream of the stagnation point to the trailing edge, allowing for the flow penetration into the inner volume in the stagnation region.

In the present study, the porous medium is assumed to be melamine foam with homogeneous and isotropic material properties as proposed in [26]. The characterization required to set up the model in Eq. (13) is described by Satcunanathan *et al.* [44], and the corresponding parameters are $\varphi = 0.986$, $Da = 5.3 \times 10^{-6}$, and $c_F = 0$. For the computation of the Darcy number, the rod diameter is considered as the reference length. In the fluid Ω_f and porous Ω_p regions, Eq. (10) is solved with the surface-filter terms from Eq. (12) and with $\boldsymbol{H}^{int}$ neglected. Instead, both domains are matched at the interface in the respective cut-cells by means of the jump conditions.

C. Computational domain

The computational domain extends $90\,d \times 64\,d \times \pi\,d$ in the streamwise, upwash, and spanwise directions, respectively, resulting in 186 million mesh points for the solid configuration and 206 million grid points for the porous one. As depicted in Fig. 1b, the grid is locally refined around solid boundaries and in the fluid-porous interface Γ around the airfoil and gradually coarsened in the outer field. The local grid spacing is here given by $\Delta_r = 144/2^{R_L}$, where R_L is the refinement level that ranges from 11 to 15, i.e., the smallest cell size is $4.39 \times 10^{-3}\,d$. Finally, periodic boundary conditions are imposed in the spanwise direction, and constant atmospheric pressure is enforced on the far-field boundaries with a sponge treatment at the outflow boundary to damp spurious waves.

D. LES data processing

The current investigation features processing the time signals of pressure, velocity, and density fluctuations over the airfoil surface and in the upstream flow. Basic expressions that will be applied to the simulated data are briefly defined in this section.

1. Flow-field and surface quantities

After the transient, the turbulent-flow field is time-averaged to calculate the related statistics at each location of the domain. These values are processed at a sampling frequency of $f_s = 25.6\,\text{kHz}$ for a total of $T_s\,U_\infty/d = 78$ time units, which corresponds to approximately 15.6 shedding cycles at a Strouhal number of $St = 0.2$ based on the rod diameter and free-stream velocity, to reach statistical convergence. The averaged and root-mean-square (r.m.s) velocities extracted along the stagnation streamline of the wing profile have been compared with hot-wire measurements in [28] to validate the numerical data.

The frequency-domain quantities employed in the subsequent sections are computed by the Welch periodogram method [45], using Hanning windows of blocks of 1×2^9 samples with 75 % overlap, thus providing a frequency resolution of approximately 48 Hz. Among these, the normalized spatial coherence between the reference time signal q_0 and generic time signal q is defined as

$$\gamma^2_{q_0 q}(f) = \frac{|\Phi_{q_0 q}(f)|^2}{\Phi_{q_0 q_0}(f)\,\Phi_{qq}(f)}, \tag{14}$$

where $\Phi_{q_0 q_0}$ denotes the power spectral density of q_0, while $\Phi_{q_0 q}$ indicates the cross spectral density between q_0 and q. From the latter, the phase difference between the two signals can be computed as

$$\phi_{q_0 q}(f) = \text{Im}\left[\Phi_{q_0 q}(f)\right]. \tag{15}$$

2. Identification of vortical structures

An effective method to identify a large-scale vortical structure immersed in the turbulent flow and interacting with the wing-profile surface is through the Γ_1 and Γ_2 scalar functions, which are based on the normal angular momentum of the instantaneous velocity field. The former is equivalent to a spatial pulse whose peak value represents the sign ± 1 of vorticity at the cores of the turbulent eddies and decays fast when moving away from them. The latter makes it possible to separate the regions dominated by the rotation rate from those dominated by the strain rate and, by doing so, provide the shape of the large vortical structures, independently of their strength. Following Graftieaux et al. [46], they are defined as

$$\Gamma_1(\boldsymbol{x}_P) = \frac{1}{N} \sum_{S_P} \frac{[(\boldsymbol{x}_P - \boldsymbol{x}_M) \times \boldsymbol{u}_M] \cdot \boldsymbol{n}_P}{(\boldsymbol{x}_P - \boldsymbol{x}_M) \cdot \boldsymbol{u}_M}; \tag{16}$$

$$\Gamma_2(\boldsymbol{x}_P) = \frac{1}{N} \sum_{S_P} \frac{[(\boldsymbol{x}_P - \boldsymbol{x}_M) \times (\boldsymbol{u}_M - \bar{\boldsymbol{u}}_P)] \cdot \boldsymbol{n}_P}{(\boldsymbol{x}_P - \boldsymbol{x}_M) \cdot (\boldsymbol{u}_M - \bar{\boldsymbol{u}}_P)}, \tag{17}$$

where P is a fixed point at the position $\boldsymbol{x}_P$, S_P is a discretised two-dimensional area surrounding P and containing N points, $\boldsymbol{n}_P$ is the unit vector normal to S_P, and $\boldsymbol{u}_M$ and $\bar{\boldsymbol{u}}_P$ are the instantaneous velocity at the generic point M and local convection velocity at the point P, respectively. The separation between the regions of dominant rotation rate and strain rate occurs for $|\Gamma_2| = 2/\pi$. The size of the area, i.e., the parameter N, plays here the role of a spatial filter, and is set to be $r_{LE} \times r_{LE}$ wide in the present study.

V. Results and discussion

In this section, the results of the analysis of Curle's dipolar sources are presented. First, the effect of porosity on the pressure fluctuations on the surface of the airfoil is evaluated. Second, the impact of the noise sources produced by the nonzero Reynolds stresses on the porous surface and their correlation with the unsteady-pressure term are discussed.

A. Unsteady-pressure term

As shown in Section II, the interaction of the upstream turbulent flow shed by the circular rod with the airfoil induces unsteady pressures on its surface. Figure 2 depicts the contours of the r.m.s. surface-pressure fluctuations for the solid and porous cases. The values are normalized by the free-stream dynamic pressure. Interestingly, the region with the highest pressure amplitudes is not located at the leading edge but slightly downstream of it. For the impermeable airfoil (Fig. 2a), the largest r.m.s. pressure fluctuations appear to be at a chordwise location of $x/r_{LE} \approx 0.47$. The possibility for the flow to permeate the body surface results in an attenuation of the peak amplitude (Fig. 2b), which is spread over a larger region. The mitigation effect of porosity on the unsteady pressure is likely responsible for the far-field noise reduction previously observed in [26–28, 30].

8

(a)   (b)
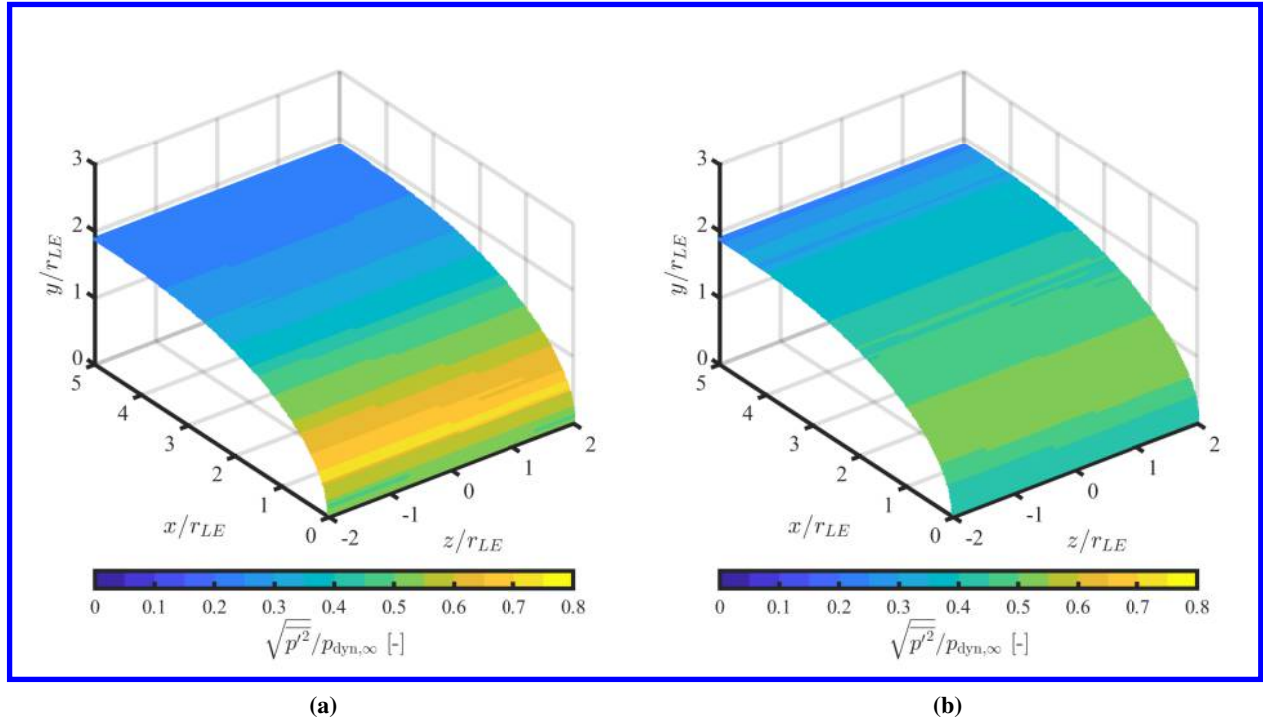
Fig. 2   R.m.s. pressure-fluctuations contours on the surface of the (a) solid and (b) porous airfoils made dimensionless by the free-stream dynamic pressure.
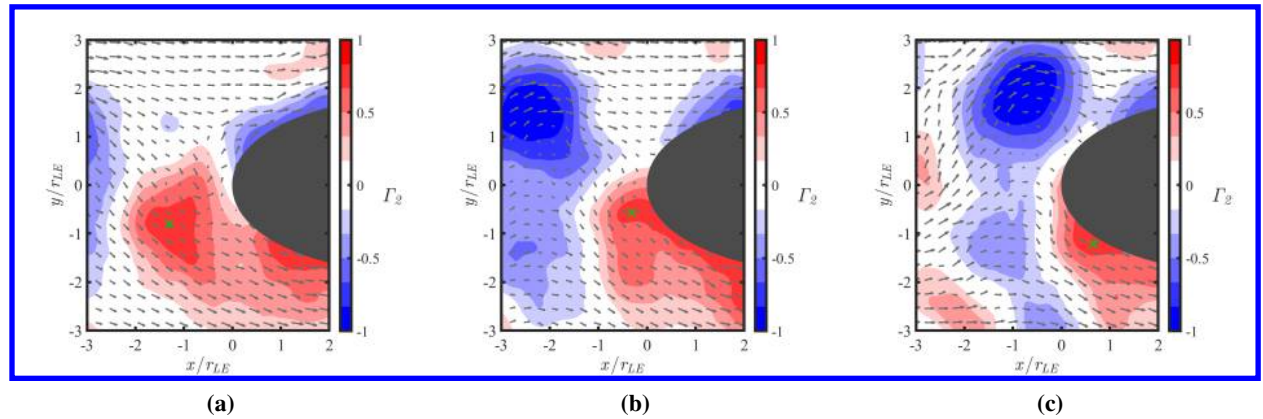

(a)   (b)   (c)

Fig. 3 Γ_2 function fields for the solid airfoil at (a) a reference time t_1, (b) a time $t_2 \approx t_1 + d/U_\infty$, and (c) a time $t_3 \approx t_1 + 2\,d/U_\infty$. The x symbol denotes the center of the highlighted turbulent structure that approaches the leading edge, which is extracted from the Γ_1 function, while the arrows indicate the vectors of the instantaneous velocity field.

A possible explanation for the downstream displacement of the peak of the r.m.s. pressure fluctuations could be attributed to the significant thickness of the NACA-0024 profile. Indeed, the leading edge of such an airfoil does not constitute a sharp geometric singularity. The turbulent structures that are advected towards the stagnation region by the mean-flow field are subjected to a strong acceleration in the area of the largest streamline curvature and impinge on the surface at higher velocities and more downstream locations. The vortex dynamics outlined here is more clearly illustrated in Fig. 3 that shows instantaneous fields of the Γ_2 function evaluated at three different time instants differing by d/U_∞. The selected time steps enable following the evolution of a vortex approaching the solid airfoil, which is initially undistorted and located upstream of the stagnation point (Fig. 3a) and subsequently interacts with the wing

9

profile (Fig. 3b), getting distorted and advected along its surface as a consequence of the airfoil blockage effect (Fig. 3c).
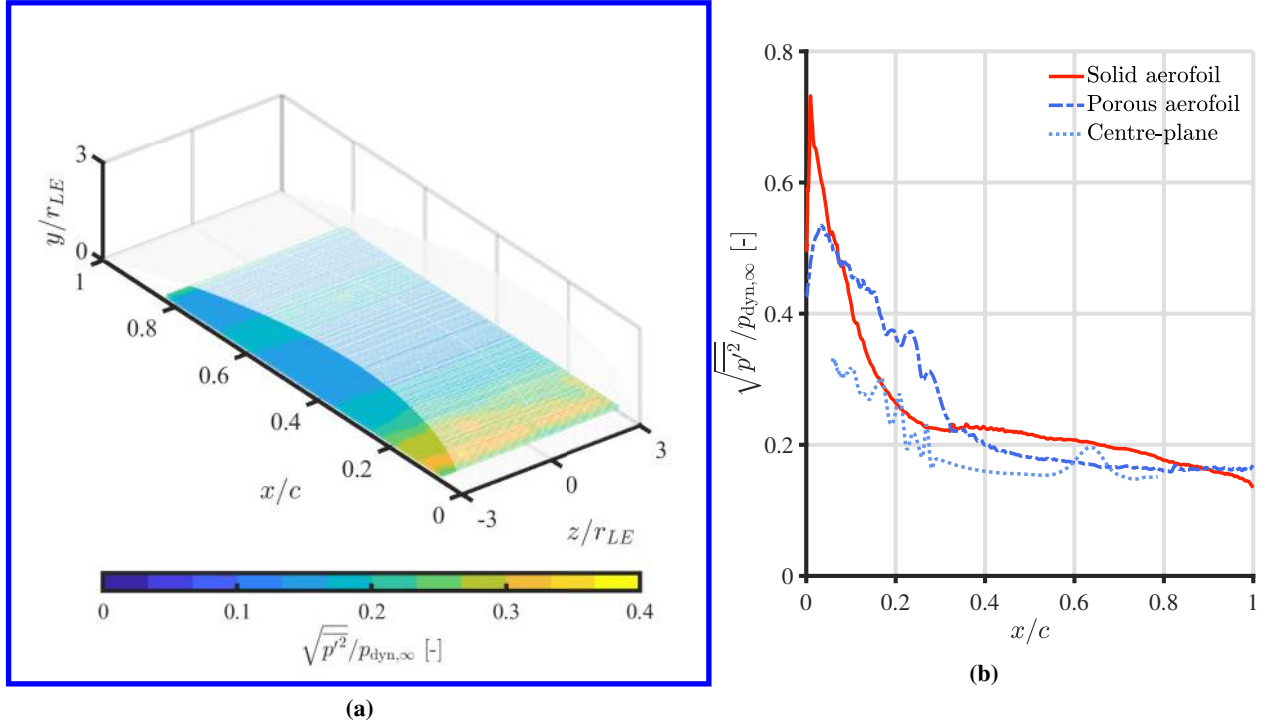

(a)

(b)

Fig. 4 **(a) Contours of r.m.s. pressure fluctuations on the centerplane of the porous airfoil. The opaque surface denotes the NACA-0024 profile. (b) R.m.s. pressure fluctuations on the surface of the solid and porous airfoils and the centerplane averaged over the span. All values are made dimensionless by the free-stream dynamic pressure.**

Furthermore, the presence of the impermeable centerplane potentially affects the acoustic field due to scattering of the pressure fluctuations generated on its surface and propagating within the porous medium [28]. The contours of the r.m.s. pressure fluctuations are presented in Fig. 4a to show the amplitude of the noise sources associated with this component. The peak in the unsteady-pressure term appears to be concentrated at the plate leading edge and decreases with increasing chordwise positions up to approximately the region of maximum thickness of the airfoil, after which it remains constant. It is important to point out that the volume-averaged continuum approach discards motions at the subfilter scale inside the porous medium. However, their contribution to the overall r.m.s. surface-pressure fluctuations can be considered negligible, as demonstrated by Breugem [47] by comparing the results of a volume-averaged direct numerical simulation with a resolved one.

The trends discussed so far are better visualized in Fig. 4b, which depicts the r.m.s. surface-pressure fluctuation profiles of the airfoils and centerplane averaged over the span. The attenuation in the unsteady-pressure peak at $x/c \approx 0.03$, corresponding to $x/r_{LE} \approx 0.47$, amounts to about 20 %. Downstream of the peak region, the surface-pressure fluctuations decay faster for the solid configuration than for the porous one up to $x/c \approx 0.4$, possibly due to the influence of the centerplane, which is found to be significant. Indeed, the chordwise position where the unsteady pressure is maximum for the porous NACA-0024 profile corresponds to the leading edge of this component. Additionally, the trend in surface-pressure fluctuations on the centerplane closely follows that of the porous airfoil, yet with a lower amplitude, up to $x/c \approx 0.6$. Downstream of this location, the two trends are comparable.

The effect of porosity on the spanwise spatial coherence $\gamma^2_{p'_0 p'}$ of the unsteady-pressure term between the midspan of the airfoil ($z/r_{LE} = 0$) and spanwise-varying locations is shown in Fig. 5. This quantity is a measure of the acoustic efficiency of a noise source [48]. Two streamwise locations are considered for the computation of γ^2, namely $x/r_{LE} = 0$, i.e., the leading edge, and $x/r_{LE} = 0.47$, i.e., the position where the largest pressure fluctuations occur. Since periodic boundary conditions have been used in the prediction of the turbulent field (see Section III), the spatial-coherence values are meaningful only for separation distances less than half the simulated span, which corresponds to approximately $3.2 \, r_{LE}$ [27]. Results are presented as a function of the Strouhal number *St* based on the cylindrical rod diameter and the free-stream velocity.
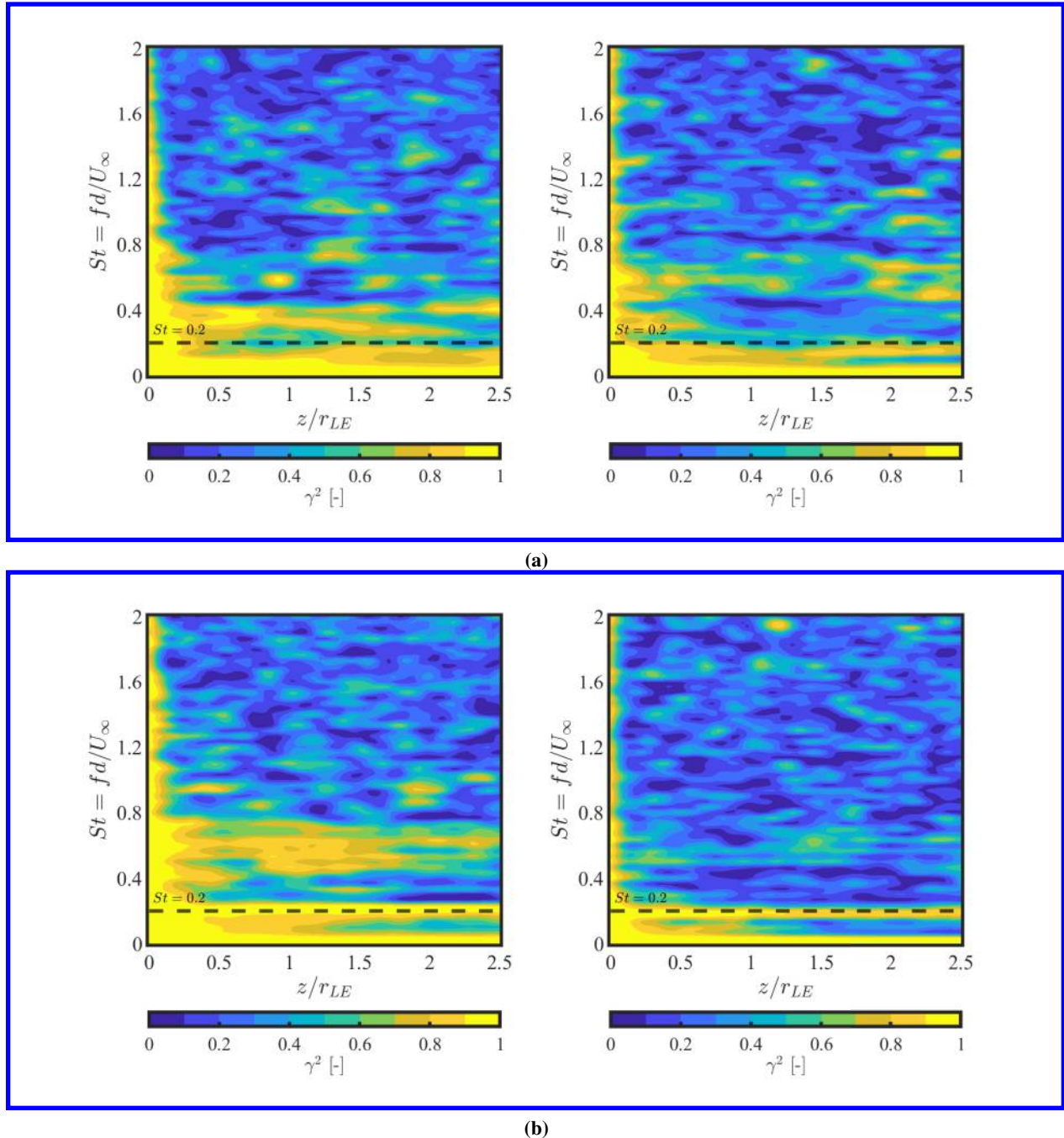
(a)

(b)

Fig. 5 Spanwise spatial-coherence contours of the pressure fluctuations on the surface of the solid (on the left) and porous (on the right) airfoils computed at (a) $x/r_{LE} = 0$ and (b) $x/r_{LE} = 0.47$. The reference is set at the midspan location ($z/r_{LE} = 0$). The dashed line indicates the Strouhal number corresponding to the vortex shedding peak.

At the airfoil leading edge (Fig. 5a), porosity appears to have an overall minor impact on the spanwise coherence. For both solid and porous configurations, γ^2 is maximum for lower St (due to the effect of the mean flow) and z and rapidly decreases with increasing frequency. The only exception occurs at the Strouhal number linked to the fluctuating drag, i.e., $St \approx 0.4$, where unsteady pressures on the impermeable wing-profile surface remain partly coherent over a distance of two leading-edge radii from midspan. The same trend is not observed for the porous case. Moreover, the
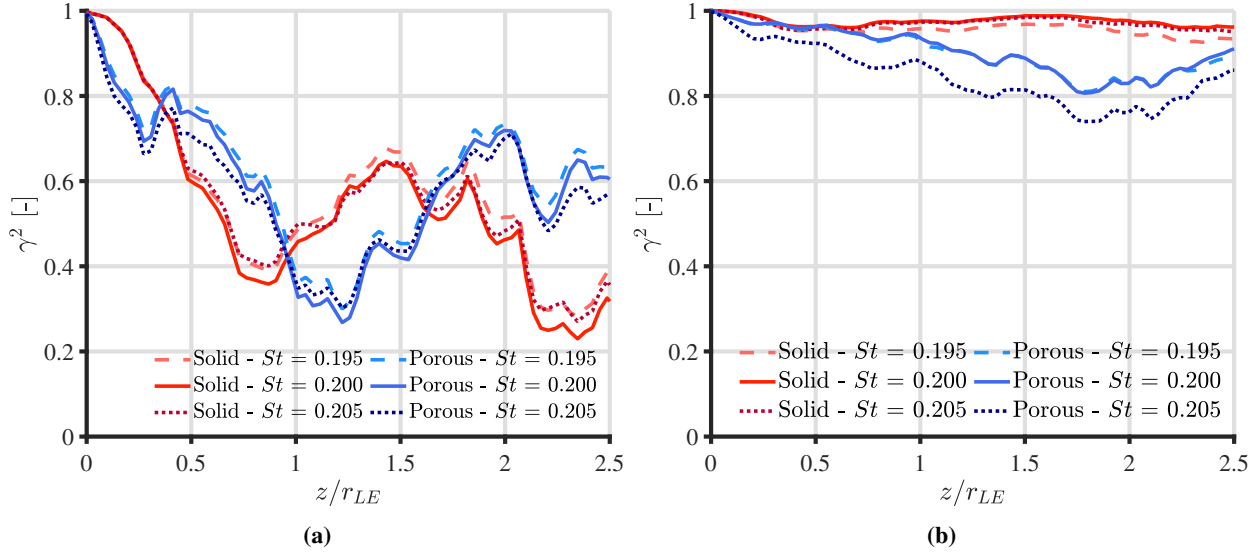
11

Fig. 6 Spanwise spatial-coherence profiles of the pressure fluctuations on the surface of the solid and porous airfoils computed at (a) $x/r_{LE} = 0$ and (b) $x/r_{LE} = 0.47$ for different interpolated Strouhal numbers in the vicinity of the vortex-shedding frequency peak. The reference is set at the midspan location ($z/r_{LE} = 0$).

contours exhibit no evident peak associated with the vortex shedding, which is instead clearly visible at the location of largest r.m.s. pressure fluctuations (Fig. 5b). Indeed, the spanwise spatial coherence of the unsteady pressure at $St = 0.2$ remains close to 1 over the whole span for both airfoils at this position. The integration of porosity only results in a marginal attenuation of this quantity but decreases the amplitude of the γ^2 peaks present in the range $0.4 < St < 0.8$ for $z/r_{LE} < 2$.

Interestingly, a slight shift of the shedding frequency towards lower Strouhal numbers occurs for the porous wing profile. This trend agrees with previous experimental observations conducted on equivalent NACA-0024 profiles [3, 30] and may be related to a different blockage exerted by the airfoil. The extraction of the spanwise spatial-coherence contours in Figs. 5a and 5b interpolated for $0.195 < St < 0.205$ allows clarifying this tendency and is illustrated in Fig. 6. While γ^2 decays over a relatively short distance for the three St under consideration at the leading edge (Fig. 6a) reaching values below 0.5 within $1\,r_{LE}$ from midspan, it remains above 0.9 for the entire span at $x/r_{LE} = 0.47$ for both airfoils (Fig. 6b). At the latter position, the possibility of the flow permeating the wing profile results in a reduction of up to 10 % in the spatial coherence. In this case, the mitigation becomes more significant for the higher Strouhal number, hinting at the aforementioned shift of the vortex-shedding peak, whereas γ^2 is the same for $St = 0.195$ and $St = 0.2$.

Additionally, the unsteady pressures on the surface of the airfoils maintain a high degree of correlation with those at the location where the largest fluctuations occur also along the chord. Figure 7 compares the spatial coherence between the solid and porous configurations at the vortex-shedding frequency peak. The reference position is the same as that in Fig. 5b. Besides the strong spanwise correlation already described above, the results for the solid configuration show that γ^2 is close to 1 over a distance of about $3\,r_{LE}$, or $0.2\,c$, from the leading edge. The present trend suggests that the region of the greatest curvature of the wing profile radiates in unison. Downstream of this location, the spatial coherence rapidly decreases, reaching approximately 0 around the position of maximum airfoil thickness, and increases again at $0.4 < x/c < 0.6$. Porosity affects γ^2 by slightly mitigating the initial high-coherence area. Furthermore, both decay at $x/c = 0.3$ and increase at $0.4 < x/c < 0.6$ are milder in this case.

In the regions where the spatial coherence of the surface-pressure fluctuations is high, the phase information of the cross-spectral densities can be evaluated to investigate potential interference effects. Figure 8 depicts the phase-difference $\phi_{p'_0 p'}$ contours of the unsteady pressures on the solid and porous airfoil surfaces computed at the vortex-shedding frequency peak. Once again, the reference point is set at midspan of $x/r_{LE} = 0.47$. Following Kim *et al.* [49], data are plotted as $\cos \phi_{p'_0 p'}$ so that the resulting values vary between 1 and -1 when the phase difference is $2m\pi$ (in phase) and $(2m + 1)\pi$ (out of phase), respectively, m being an integer number. For both wing profiles, surface-pressure fluctuations are perfectly in phase in the region of greatest curvature of the NACA-0024 models, i.e., where γ^2 is maximum. These conditions constitute the base for efficient sound production. At the location of maximum thickness of the airfoil, the
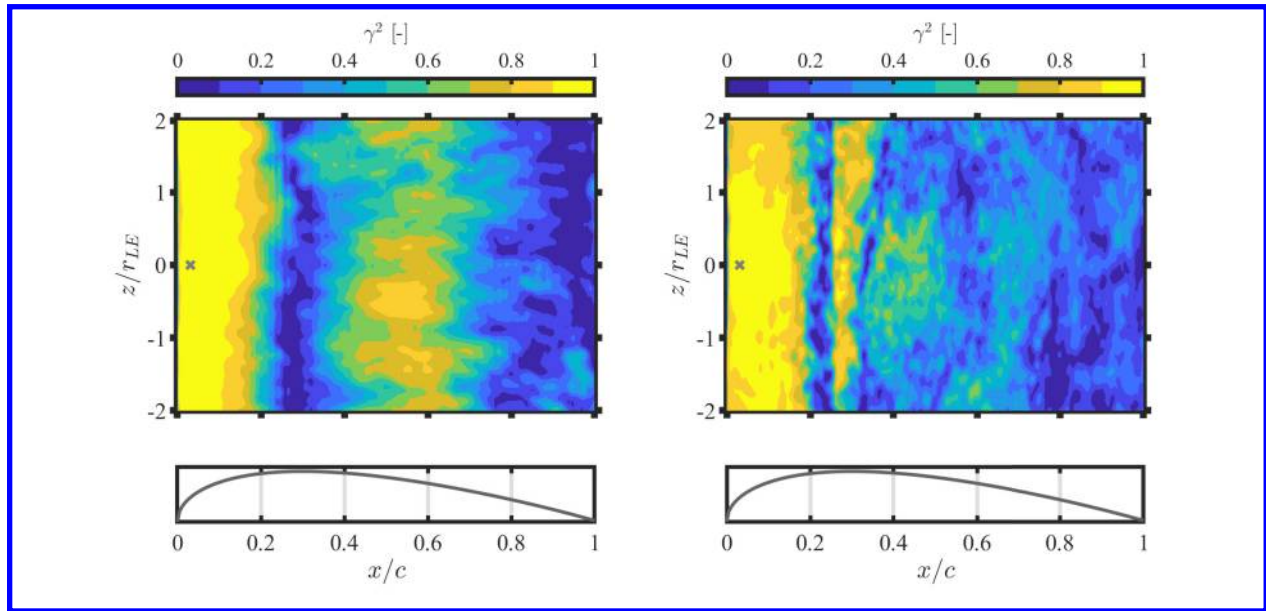
Fig. 7 **Spatial-coherence contours of the pressure fluctuations on the surface of the solid (on the left) and porous (on the right) airfoils at** $St = 0.2$. **The reference is set at the location** $(x/r_{LE}; z/r_{LE}) = (0.47; 0)$, **marked by the symbol** x.
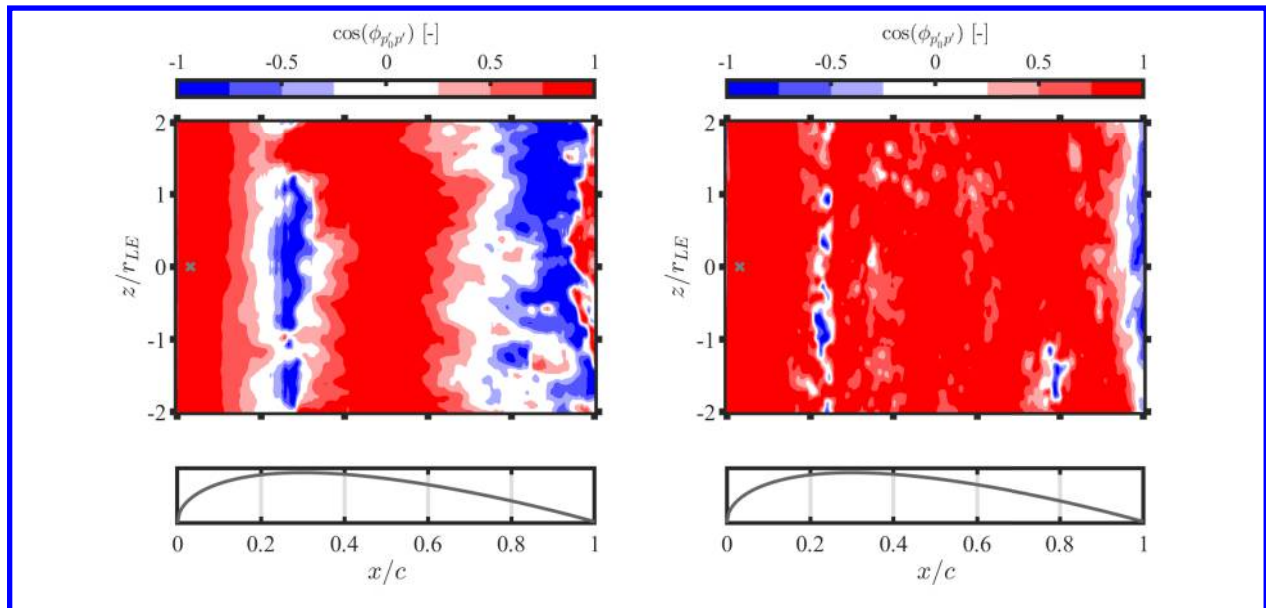

Fig. 8 **Phase-difference contours of the pressure fluctuations (expressed using the cosine function) on the airfoil surface at** $St = 0.2$ **for the solid (on the left) and porous (on the right) configurations. The reference is set at the location** $(x/r_{LE}; z/r_{LE}) = (0.47; 0)$, **marked by the symbol** x.

degree of destructive phase interference increases significantly for the impermeable configuration, in correspondence with the low-coherence area visible in Fig. 7. The same correlation between $\cos \phi_{p'_0 p'} \approx -1$ and $\gamma^2 \approx 0$ is also found for the porous wing profile, for which the level of constructive phase interference is high throughout the entire surface.

A better insight into the physical mechanisms that induce the unsteady-pressure term is provided by evaluating the spectral content of the surface-pressure fluctuations and the turbulent velocities in the vicinity of the wing profiles. Such a comparison is reported in Fig. 9, where the power spectral densities of the aforementioned quantities are plotted for
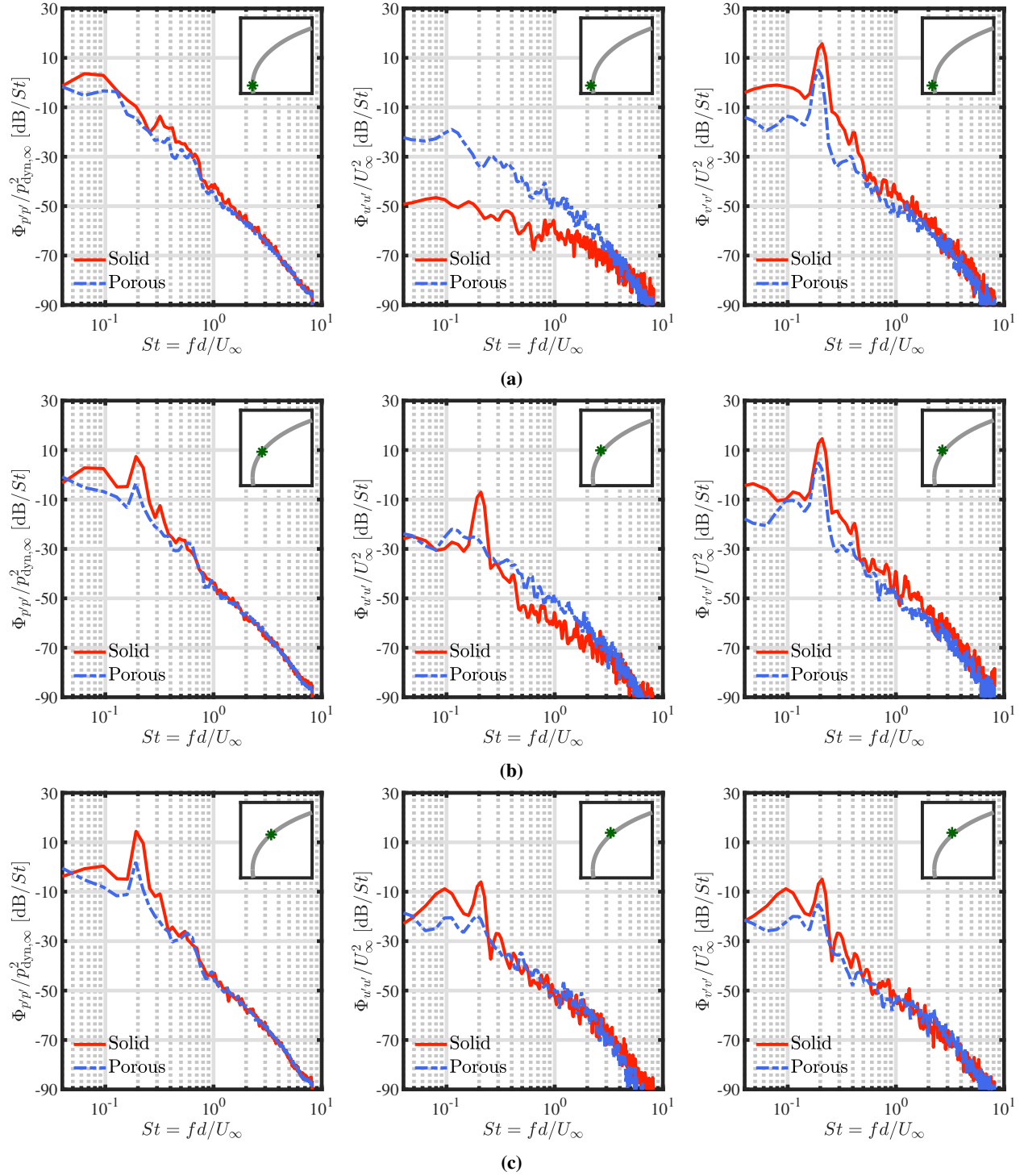
13

Fig. 9 Power spectral densities of the unsteady-pressure fluctuations and the streamwise and upwash velocity fluctuations for the solid and porous airfoils averaged over the span. The pressures are extracted at (a) $x/r_{LE} = 0$**, (b)** $x/r_{LE} = 0.24$**, and (c)** $x/r_{LE} = 0.47$**, whereas the velocities at a distance of** $0.05\,r_{LE}$ **from these locations considering the normal to the surface. The initial data are normalized by the corresponding free-stream values.**

the solid and porous airfoils. Three chordwise positions ranging from the leading edge to the source peak are considered for the extraction of the surface-pressure data, namely $x/r_{LE} = 0$, $x/r_{LE} = 0.24$, and $x/r_{LE} = 0.47$. The corresponding

locations at which velocity spectra are estimated lie at a distance of $0.05\,r_{LE}$ from the body considering the normal to the surface, by analogy with the analysis carried out by Zamponi *et al.* [28]. The power spectral densities are averaged over the span and normalized by U_∞^2 and $p_{\mathrm{dyn},\infty}^2$, such that the different quantities can be directly compared.

At the leading edge (Fig. 9a), $\Phi_{p'p'}$ and $\Phi_{u'u'}$ for both airfoils do not exhibit any peak at $St = 0.2$, in contrast to $\Phi_{v'v'}$. The presence of porosity results in a mild attenuation in the pressure spectra at low frequencies and a reduction in the momentum transfer between the streamwise and upwash velocity fluctuations, which mitigates the decrease in u' and increase in v' from their upstream, undistorted values [28]. At $x/r_{LE} = 0.24$ (Fig. 9b), the vortex-shedding peak appears in the $\Phi_{p'p'}$ spectra for both configurations. A low-frequency attenuation is present also in this case due to the porous treatment of the wing profile. $\Phi_{u'u'}$ still exhibits higher values for the porous airfoil than for the solid one, yet with a minor discrepancy, and the peak at $St = 0.2$ is visible only for the latter. Likewise, the reduction in $\Phi_{v'v'}$ induced by porosity is lower. At $x/r_{LE} = 0.47$ (Fig. 9c), the results follow the trends discussed above. The vortex-shedding peak in the surface-pressure spectra is more evident, while the deviations between solid and porous configurations in the velocity spectra are further mitigated, leading to a comparable trend for the two components. Moreover, a slight shift of the vortex-shedding peak towards lower St occurs for all power spectral densities, in agreement with what has been observed in Fig. 6b.
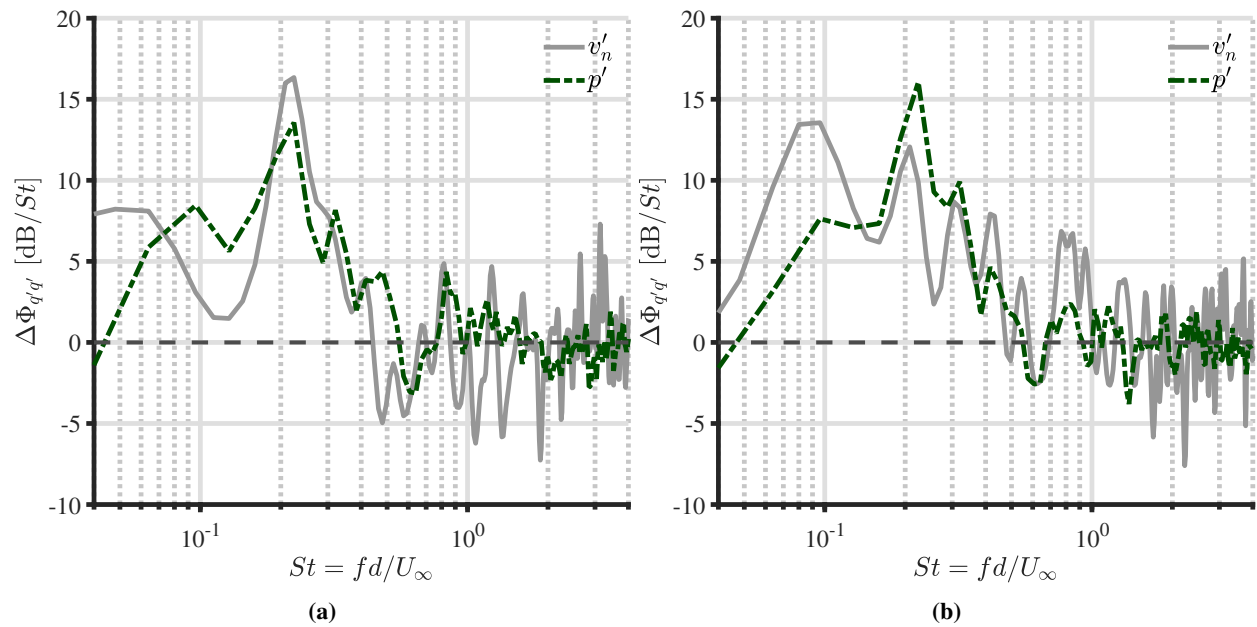

Fig. 10 Difference of the power spectral densities of the unsteady surface pressures and normal velocity fluctuations averaged over the span between the solid and porous airfoils, where q is the generic term. The pressure is extracted at (a) $x/r_{LE} = 0.24$ and (b) $x/r_{LE} = 0.47$, whereas the velocity at a distance of $0.05\,r_{LE}$ normal to the surface from these locations.

Interestingly, the frequency range at which porosity has an impact on the spectra is similar for $\Phi_{p'p'}$, $\Phi_{u'u'}$, and $\Phi_{v'v'}$ for the locations downstream of the leading edge. The results presented in Fig. 9 suggest that a potential link exists between the unsteady pressure on the surface and nearby unsteady velocity u_n that is perpendicular to it. This scenario is consistent with the analysis carried out by Panton and Linebarger [50] and would explain why at the stagnation point, where the normal $\boldsymbol{n}$ is parallel to the incoming flow, the vortex-shedding frequency peak in the pressure spectra is not visible, in accordance with the conclusions drawn on the spatial coherence in Fig. 5a. Figure 10 illustrates the relative power spectral densities of these two quantities, which are calculated as deviation between the solid and porous cases at $x/r_{LE} = 0.24$ and $x/r_{LE} = 0.47$. Positive values indicate a decrease in the spectra due to porosity, whereas negative ones denote an increase. For both locations, a notable agreement between $\Delta\Phi_{p'p'}$ and $\Delta\Phi_{u_n'u_n'}$ can be observed for most of the spectrum, which shows that the porous treatment reduces the power-spectral-density levels up to $St \approx 0.6$, with the maximum abatement occurring at the vortex-shedding frequency. This correspondence suggests that the physical mechanisms behind the turbulence-distortion attenuation proposed by Zamponi *et al.* [32] using the RDT are also responsible for mitigating the pressure fluctuations on the airfoil surface. In other words, porosity decreases the

15

changes in the turbulent-flow field produced by the presence of the body and, in turn, the reaction force exerted by it due to unsteady incident velocity. This phenomenon constitutes the dominant noise-reduction mechanism of the porous treatment of the wing profile and confirms the hypotheses formulated in previous works [3, 28, 30, 32].
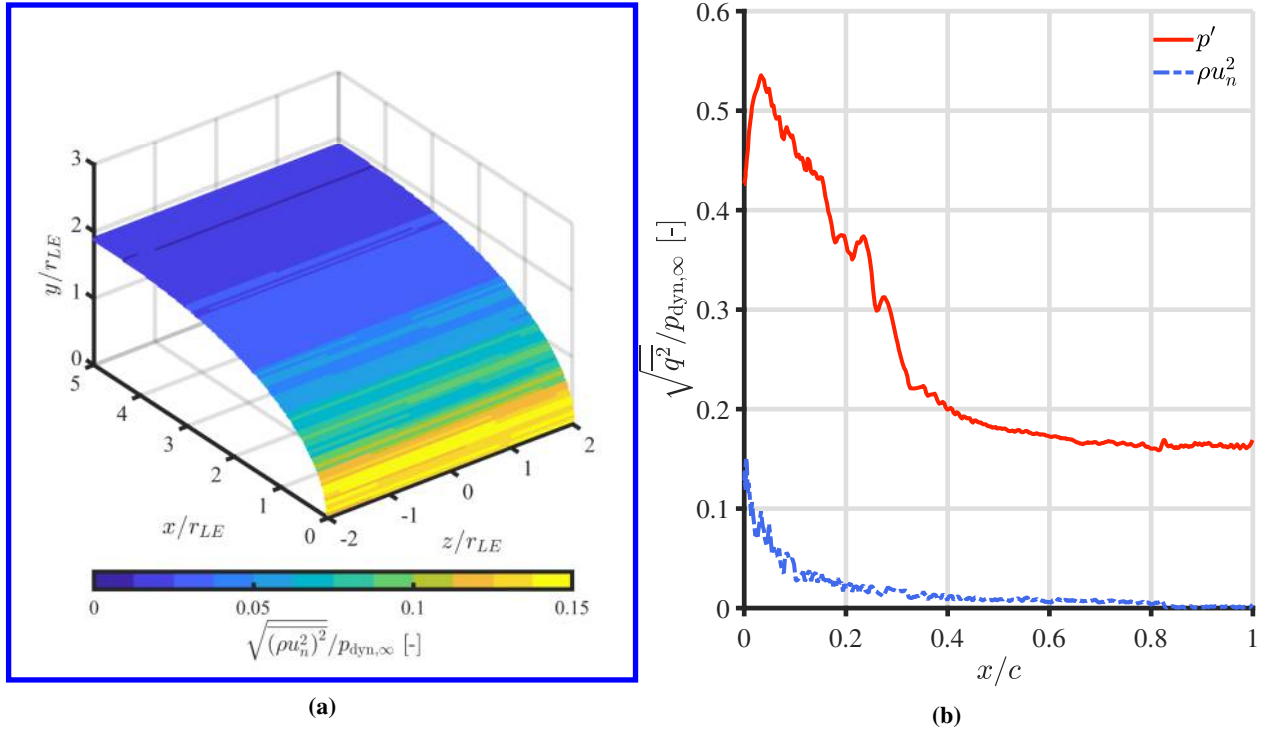
B. Reynolds-stresses term

(a)

(b)

Fig. 11 **(a) R.m.s. Reynolds-stresses ρu_n^2 contours on the porous airfoil surface. (b) R.m.s. Reynolds-stresses ρu_n^2 and unsteady-pressure p' profiles averaged over the span of the porous airfoil surface. q is the generic term. All terms are made dimensionless by the free-stream dynamic pressure.**

The presence of a transpiration velocity at the surface of the porous airfoil implies that nonzero Reynolds stresses appear on it. According to Eq. (8), the far-field acoustic pressure associated with this source has a dipolar nature, and its relative contribution to the overall noise emitted by a porous wing profile has not been addressed in the literature. The investigation of the amplitude and correlation of the Reynolds-stresses term can shed light upon this influence and constitutes the topic of the present section. In the analyses performed below, the vector $\rho u_n \boldsymbol{u}$ from Eq. (8) is projected along the normal to the body to allow for a direct comparison with the surface-pressure fluctuations.

The rate of airflow penetrating the wing profile affects substantially the magnitude of the Reynolds-stresses term that is thus expected to be maximum in the stagnation region. This supposition is verified by the normalized r.m.s. contours of ρu_n^2 on the porous airfoil surface depicted in Fig. 11a, which highlights that the source peak is located close to the leading edge, at $x/r_{LE} \approx 0.06$, and rapidly decreases with the increasing chordwise position. However, its amplitude is considerably smaller than that of the unsteady-pressure term. Figure 11b compares r.m.s. profiles for ρu_n^2 and p' averaged along the airfoil span and provides a visualization of such difference. Results show that the peak in p' amounts to approximately three times the peak in ρu_n^2. Moreover, the Reynolds-stresses term decays faster than the unsteady-pressure one, becoming negligible for $x/c > 0.1$.

By analogy with the studies presented in Section V.A, the acoustic efficiency of the noise source associated with ρu_n^2 can be investigated by looking at the spanwise spatial coherence in Fig. 12a. In this case, γ^2 is evaluated at the location where the maximum r.m.s. values of the Reynolds stresses occur, i.e., $x/r_{LE} \approx 0.06$, with a reference set at the airfoil midspan. Once again, a clear peak at the vortex-shedding frequency appears, yet with a lower intensity and extension than for the surface-pressure fluctuations, as visible in the corresponding γ^2 profiles extracted for $0.195 < St < 0.205$ in Fig. 12b. These trends show that an abrupt loss of spatial coherence is found at a distance of about $2 r_{LE}$ from the
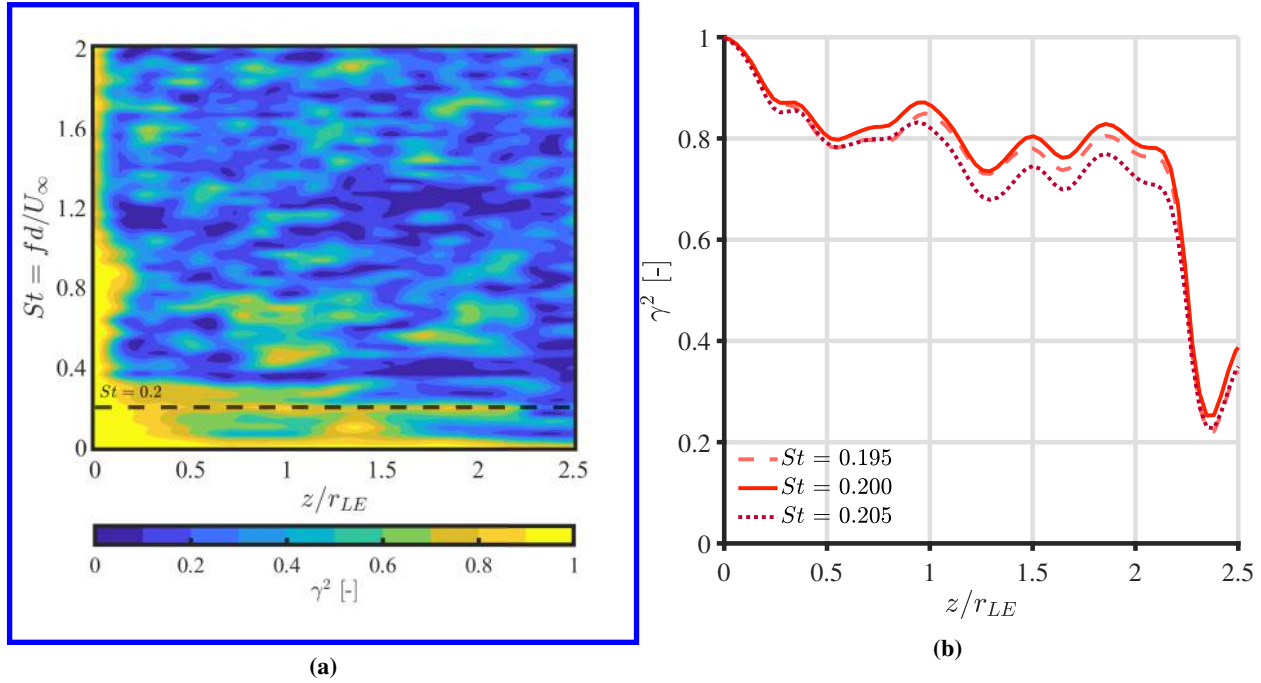
16

Fig. 12   (a) Spanwise spatial-coherence contours of the Reynolds stresses ρu_n^2 **on the surface of the porous airfoil computed at** $x/r_{LE} = 0.06$**. (b) Spanwise spatial-coherence profiles of** ρu_n^2 **on the surface of the porous airfoil computed at** $x/r_{LE} = 0.06$ **for different interpolated Strouhal numbers in the vicinity of the vortex-shedding frequency peak. The reference is set at the midspan location (**$z/r_{LE} = 0$**).**

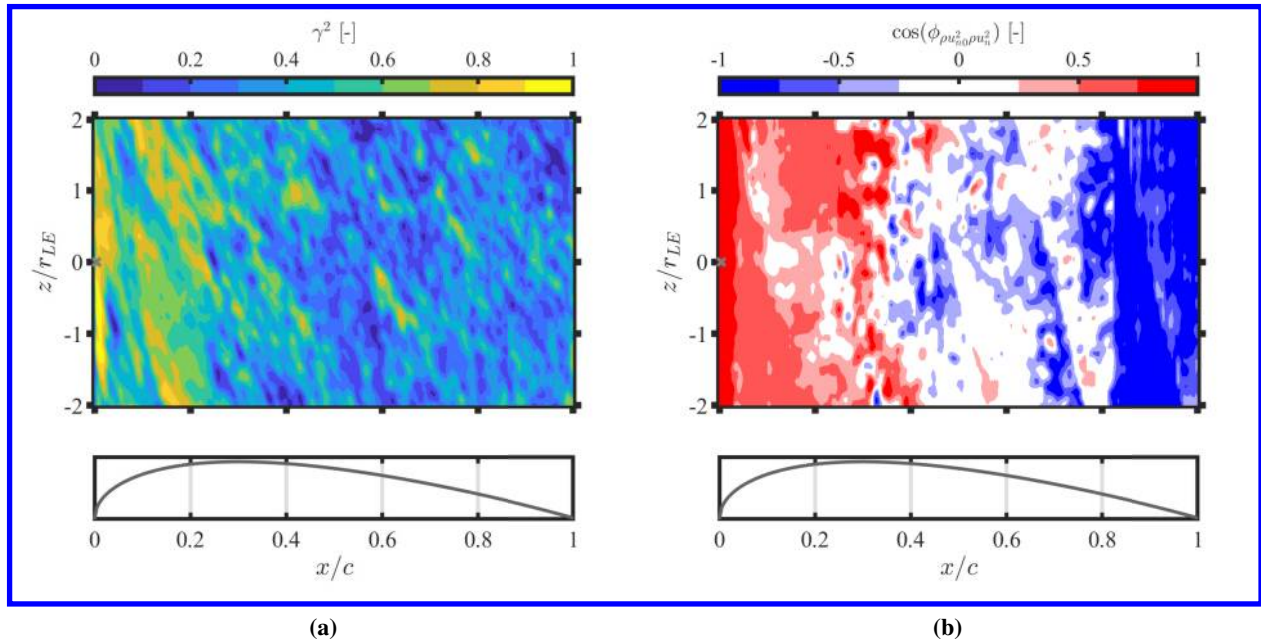midspan, independently of the considered Strouhal number.

Fig. 13   (a) Spatial-coherence and (b) phase-difference (expressed with the cosine function) contours of the Reynolds stresses ρu_n^2 **on the surface of the porous airfoil at** $St = 0.2$**. The reference is set at the location** $(x/r_{LE}; z/r_{LE}) = (0.06; 0)$**, marked by the symbol** x**.**

17

Furthermore, a relatively poor correlation is maintained with the sources downstream of the peak position. Figure 13a illustrates the spatial coherence of ρu_n^2 computed at $St = 0.2$ along the porous airfoil surface. The reference location is consistent with that of Fig. 12. Results reveal that the region of high γ^2 is concentrated near the leading edge, where the transpiration velocity is larger. For $x/c > 0.3$, the correlation becomes negligible. Similar conclusions can be drawn for the corresponding phase difference reported in Fig. 13b, which are calculated considering a reference at $(x/r_{LE}; z/r_{LE}) = (0.06; 0)$. In this case, the noise sources in the stagnation region are in phase and expected to radiate in unison, whereas those downstream of the maximum airfoil thickness most likely do not contribute to the overall noise, also considering the much lower amplitudes reported in Fig. 11.

Despite the minor strength and source correlation of the Reynolds-stresses term with respect to the unsteady-pressure one, the former can potentially interfere constructively with the latter and increase the overall noise emitted by the porous airfoil. This scenario is particularly relevant in the stagnation region, where the largest Reynolds stresses occur. In Fig. 14a, the spatial coherence profile of p' and ρu_n^2 computed at the leading edge of the porous airfoil is depicted.
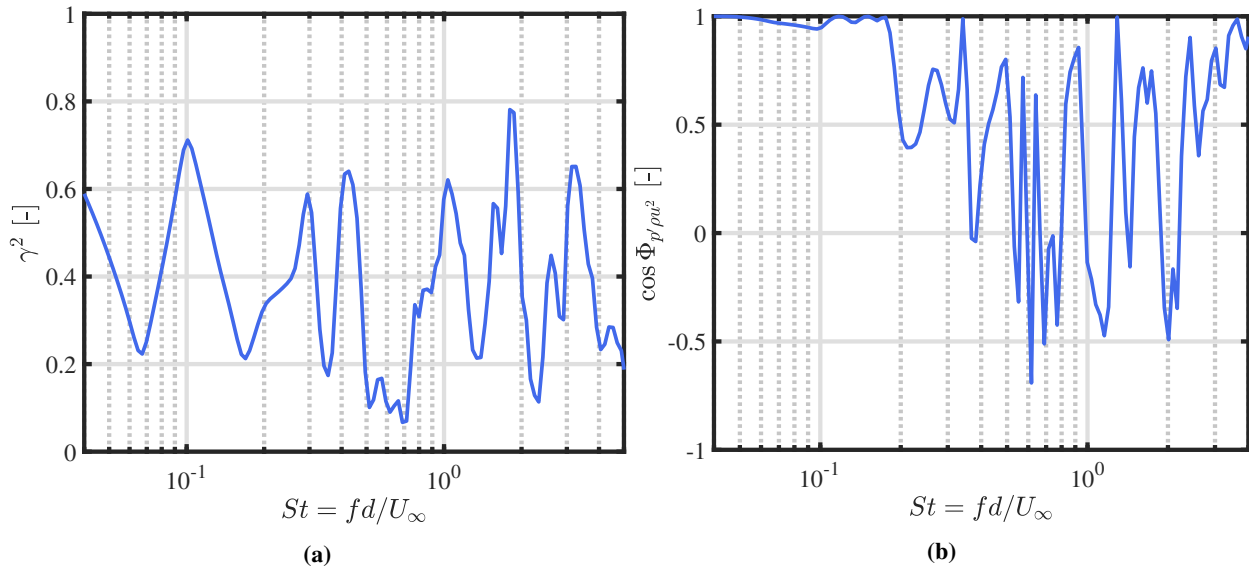

Fig. 14   (a) Spatial-coherence and (b) phase-difference (expressed with the cosine function) profiles of the unsteady-pressure and Reynolds-stresses terms at the leading edge of the porous airfoil.

For the whole frequency range, γ^2 varies between 0.2 and 0.7, hence highlighting a partial correlation between the two terms at this location. In addition, the phase-difference profiles in Fig. 14b show that p' and ρu_n^2 are in phase for low Strouhal numbers and in quadrature, i.e., $\cos(\phi_{p'\rho u_n^2}) \approx 0$ and $\phi_{p'\rho u_n^2} \approx \pi/2$, for $St > 0.2$.

VI. Concluding remarks

The present research work aims at evaluating the impact of porosity on the noise sources generated on the surface of a thick airfoil interacting with incoming turbulence. When a porous body is considered in the formulation of Curle's analogy for a compact source region, an equivalent dipolar source associated with the unsteady Reynolds stresses appears in addition to the dipole related to the surface-pressure fluctuations. Both terms have been investigated through validated LES of solid and porous NACA-0024 profiles immersed in the wake of an upstream circular rod at a Reynolds number based on the cylinder diameter of $Re_d = 4.1 \times 10^4$.

Results show that the maximum r.m.s. pressure fluctuations on the airfoil surface occur in the region of the greatest curvature due to the accelerating flow that makes the advected turbulent structures interact with the body at higher velocities. Porosity notably decreases their peak amplitude but spreads them over a larger downstream region. Moreover, the presence of a solid centerplane that prevents the crossflow between the two sides of the wing profile potentially contributes to the radiated noise by scattering the unsteady pressures on its surface through the porous medium. The analysis of the spatial coherence and phase difference reveals that, downstream of the leading edge, the pressure fluctuations maintain a high degree of correlation and in-phase behavior throughout the span for both airfoils at $St = 0.2$. This trend extends up to the 20 % of the chord, suggesting that the region of the greatest curvature of the airfoil radiates

in unison. Additionally, a slight shift in the vortex-shedding frequency peak is found for the porous configuration, possibly linked to a change in the blockage exerted by the wing profile. The spectral content of the surface-pressure fluctuations indicates that the softened distortion experienced by turbulence in the vicinity of the porous surface also causes attenuation in the unsteady pressures. A remarkable agreement is found between the decrease in the power spectral densities of the pressure fluctuations on the surface and the normal component of the turbulent velocity close to it. This important finding further confirms the hypotheses on the role of turbulence distortion in the leading-edge noise mitigation due to porosity formed in previous works.

The Reynolds-stresses term on the surface is found to be more relevant in the stagnation region of the wing profile, where the transpiration velocity is larger. Downstream of the 10 % of the chord, they become negligible. Likewise, they maintain a high degree of correlation and in-phase behavior at the vortex-shedding frequency peak. Despite their r.m.s. amplitude being considerably smaller than the unsteady-pressure term, mainly due to the low static permeability of the melamine foam, a partial correlation between the two sources is present in the stagnation region, highlighting constructive interference. This potentially decreases the effectiveness of the porous treatment by adding an additional noise source that contributes to the far-field noise.

Finally, it should be reminded that these considerations have been deduced from results obtained for a relatively thick wing profile. A thinner airfoil may exhibit different contributions of the unsteady-pressure and Reynolds-stresses terms. Nevertheless, the authors believe that the deeper understanding gained in this study will be instrumental in assessing and improving the potential of advanced porous materials for noise reduction in industrial applications.

Acknowledgements

References

[1] Kaji, S., and Okazaki, T., "Generation of sound by rotor-stator interaction," *Journal of Sound and Vibration*, Vol. 13, No. 3, 1970, pp. 281–307. https://doi.org/10/fmr3m4.

[2] Moreau, S., "Turbomachinery Noise Predictions: Present and Future," *Acoustics*, Vol. 1, 2019, p. 92. https://doi.org/10.3390/acoustics1010008.

[3] Zamponi, R., "Investigation of turbulence-surface interaction noise mechanisms and their reduction using porous materials," Ph.D. thesis, Delft University of Technology, Apr. 2021. https://doi.org/10.4233/uuid:d332c7e3-87be-4ed6-aa71-e629ef77e07a.

[4] Goldstein, M. E., "Unsteady vortical and entropic distortions of potential flows round arbitrary obstacles," *Journal of Fluid Mechanics*, Vol. 89, 1978, p. 433. https://doi.org/10/fh8tsw.

[5] Lighthill, M. J., "On sound generated aerodynamically I. General theory," *Proceedings of the Royal Society of London. Series A. Mathematical and Physical Sciences*, Vol. 211, No. 1107, 1952, pp. 564–587. https://doi.org/10.1098/rspa.1952.0060.

[6] Curle, N., "The influence of solid boundaries upon aerodynamic sound," *Proceedings of the Royal Society of London. Series A. Mathematical and Physical Sciences*, Vol. 231, No. 1187, 1955, pp. 505–514. https://doi.org/10.1098/rspa.1955.0191.

[7] Lee, S., "Reduction of blade-vortex interaction noise through porous leading edge," *AIAA Journal*, Vol. 32, No. 3, 1994, pp. 480–488. https://doi.org/10.2514/3.12011.

[8] Geyer, T., Sarradj, E., Giesler, J., and Hobracht, M., "Experimental assessment of the noise generated at the leading edge of porous airfoils using microphone array techniques," *17th AIAA/CEAS Aeroacoustics Conference (32nd AIAA Aeroacoustics Conference)*, American Institute of Aeronautics and Astronautics, Portland, Oregon, 2011. https://doi.org/10.2514/6.2011-2713.

[9] Geyer, T., Sarradj, E., and Giesler, J., "Application of a Beamforming Technique to the Measurement of Airfoil Leading Edge Noise," *Advances in Acoustics and Vibration*, Vol. 2012, 2012, pp. 1–16. https://doi.org/10/gb8jt3.

[10] Sarradj, E., and Geyer, T., "Symbolic regression modeling of noise generation at porous airfoils," *Journal of Sound and Vibration*, Vol. 333, No. 14, 2014, pp. 3189–3202. https://doi.org/10.1016/j.jsv.2014.02.037.

[11] Mineck, R. E., and Hartwich, P. M., "Effect of Full-Chord Porosity on Aerodynamic Characteristics of the NACA 0012 Airfoil," Technical Publication NASA/TP-3591, 1996.

[12] Sarradj, E., and Geyer, T., "Noise Generation by Porous Airfoils," *13th AIAA/CEAS Aeroacoustics Conference (28th AIAA Aeroacoustics Conference)*, American Institute of Aeronautics and Astronautics, Rome, Italy, 2007. https://doi.org/10.2514/6.2007-3719.

[13] Teruna, C., Avallone, F., Casalino, D., and Ragni, D., "Numerical investigation of leading edge noise reduction on a rod-airfoil configuration using porous materials and serrations," *Journal of Sound and Vibration*, 2020, p. 115880. https://doi.org/10.1016/j.jsv.2020.115880.

[14] Geyer, T. F., Lucius, A., Schrödter, M., Schneider, M., and Sarradj, E., "Reduction of Turbulence Interaction Noise Through Airfoils With Perforated Leading Edges," *Acta Acustica united with Acustica*, Vol. 105, No. 1, 2019, pp. 109–122. https://doi.org/10.3813/AAA.919292.

[15] Tamaro, S., Zamponi, R., and Schram, C., "Development of a didactic demonstrator for flow-induced noise mechanisms and mitigation technologies," *Journal of Acoustical Society of America*, Vol. 151, 2022, p. 898. https://doi.org/10.1121/10.0009366.

[16] Roger, M., Schram, C., and de Santana, L., "Reduction of Airfoil Turbulence-Impingement Noise by Means of Leading-Edge Serrations and/or Porous Material," *19th AIAA/CEAS Aeroacoustics Conference*, American Institute of Aeronautics and Astronautics, Berlin, Germany, 2013. https://doi.org/10.2514/6.2013-2108.

[17] Roger, M., and Moreau, S., "Airfoil Turbulence-Impingement Noise Reduction by Porosity or Wavy Leading-Edge Cut: Experimental Investigations," *45th International Congress and Exposition on Noise Control Engineering*, Institute of Noise Control Engineering, Hamburg, Germany, 2016, pp. 6366–6375.

[18] Bampanis, G., and Roger, M., "On the Turbulence-Impingement Noise of a NACA-12 Airfoil with Porous Inclusions," *26th AIAA/CEAS Aeroacoustics Conference*, American Institute of Aeronautics and Astronautics, Virtual event, 2020. https://doi.org/10.2514/6.2020-2577.

[19] Paruchuri, C., Joseph, P., Chong, T. P., Priddin, M., and Ayton, L. J., "On the noise reduction mechanisms of porous aerofoil leading edges," *Journal of Sound and Vibration*, Vol. 485, 2020, p. 115574. https://doi.org/10.1016/j.jsv.2020.115574.

[20] Palleja-Cabre, S., Paruchuri, C. C., Joseph, P., Priddin, M. J., and Ayton, L. J., "Downstream Perforations for the Reduction of Turbulence-Aerofoil Interaction Noise: Part I - Experimental Investigation," *AIAA AVIATION 2021 FORUM*, American Institute of Aeronautics and Astronautics, VIRTUAL EVENT, 2021. https://doi.org/10/gmght5.

[21] Priddin, M. J., Ayton, L. J., Palleja-Cabre, S., Chaitanya, P., and Joseph, P., "Downstream Perforations for the Reduction of Turbulence-Aerofoil Interaction Noise: Part II - Theoretical Investigation," *AIAA AVIATION 2021 FORUM*, American Institute of Aeronautics and Astronautics, VIRTUAL EVENT, 2021. https://doi.org/10/gmght7.

[22] Ayton, L. J., Colbrook, M. J., Geyer, T., Chaitanya, P., and Sarradj, E., "Reducing aerofoil–turbulence interaction noise through chordwise-varying porosity," *Journal of Fluid Mechanics*, Vol. 906, 2021, p. A1. https://doi.org/10.1017/jfm.2020.746.

[23] Roger, M., and Moreau, S., "Back-scattering correction and further extensions of Amiet's trailing-edge noise model. Part 1: theory," *Journal of Sound and Vibration*, Vol. 286, No. 3, 2005, pp. 477–506. https://doi.org/10.1016/j.jsv.2004.10.054.

[24] Moreau, S., and Roger, M., "Back-scattering correction and further extensions of Amiet's trailing-edge noise model. Part II: Application," *Journal of Sound and Vibration*, Vol. 323, No. 1-2, 2009, pp. 397–425. https://doi.org/10.1016/j.jsv.2008.11.051.

[25] Ayton, L. J., Karapiperis, O., Awasthi, M., Moreau, D., and Doolan, C. J., "Spanwise varying porosity for the enhancement of leading-edge noise reduction," *AIAA AVIATION 2021 FORUM*, ???? https://doi.org/10.2514/6.2021-2191.

[26] Zamponi, R., Ragni, D., Van de Wyer, N., and Schram, C., "Experimental Investigation of Airfoil Turbulence-Impingement Noise Reduction Using Porous Treatment," *25th AIAA/CEAS Aeroacoustics Conference*, American Institute of Aeronautics and Astronautics, Delft, The Netherlands, 2019. https://doi.org/10.2514/6.2019-2649.

[27] Satcunanathan, S., Meinke, M. H., and Schröder, W., "Prediction of Noise Mitigation by Porous Media based on a Direct-Hybrid CFD/CAA Method," *25th AIAA/CEAS Aeroacoustics Conference*, American Institute of Aeronautics and Astronautics, Delft, The Netherlands, 2019. https://doi.org/10.2514/6.2019-2696.

[28] Zamponi, R., Satcunanathan, S., Moreau, S., Ragni, D., Meinke, M., Schröder, W., and Schram, C., "On the role of turbulence distortion on leading-edge noise reduction by means of porosity," *Journal of Sound and Vibration*, Vol. 485, 2020, p. 115561. https://doi.org/10.1016/j.jsv.2020.115561.

[29] Zamponi, R., Moreau, S., Ragni, D., and Schram, C. F., "Experimental and Analytical Investigation of the Distortion of Turbulence Interacting with a Porous Airfoil," *AIAA AVIATION 2021 FORUM*, American Institute of Aeronautics and Astronautics, VIRTUAL EVENT, 2021. https://doi.org/10/gnrf95.

[30] Tamaro, S., Zamponi, R., Ragni, D., Teruna, C., and Schram, C., "Experimental investigation of turbulent coherent structures interacting with a porous airfoil," *Experiments in Fluids*, Vol. 62, 2021, p. 94. https://doi.org/10.1007/s00348-021-03170-2.

[31] Hunt, J. C. R., "A theory of turbulent flow round two-dimensional bluff bodies," *Journal of Fluid Mechanics*, Vol. 61, No. 4, 1973, pp. 625–706. https://doi.org/10.1017/S0022112073000893.

[32] Zamponi, R., Moreau, S., and Schram, C., "Rapid distortion theory of turbulent flow around a porous cylinder," *Journal of Fluid Mechanics*, Vol. 915, 2021, p. A27. https://doi.org/10.1017/jfm.2021.8.

[33] Glegg, S. A. L., and Devenport, W., *Aeroacoustics of low Mach number flows: fundamentals, analysis, and measurement*, Academic Press, London, 2017.

[34] Goldstein, M. E., *Aeroacoustics*, NASA SP, Scientific and Technical Information Office, National Aeronautics and Space Administration, 1974.

[35] Whitaker, S., *The Method of Volume Averaging*, Theory and Applications of Transport in Porous Media, Vol. 13, Springer Netherlands, Dordrecht, 1999. https://doi.org/10.1007/978-94-017-3389-2.

[36] Breugem, W., Boersma, B., and Uittenbogaard, R., "The influence of wall permeability on turbulent channel flow," *Journal of Fluid Mechanics*, Vol. 562, 2006, pp. 35–72. https://doi.org/10.1017/S0022112006000887.

[37] Whitaker, S., "Flow in Porous Media I: A Theoretical Derivation of Darcy's Law," *Transport Porous Media*, Vol. 1, 1986, pp. 3–25. https://doi.org/10.1007/BF01036523.

[38] Whitaker, S., "The Forchheimer equation: A theoretical development," *Transport Porous Media*, Vol. 25, No. 1, 1996, pp. 27–61. https://doi.org/10.1007/BF00141261.

[39] Schneiders, L., Hartmann, D., Meinke, M., and Schröder, W., "An accurate moving boundary formulation in cut-cell methods," *Journal of Computational Physics*, Vol. 235, 2013, pp. 786–809. https://doi.org/0.1016/j.jcp.2012.09.038.

[40] Jacob, M. C., Boudet, J., Casalino, D., and Michard, M., "A rod-airfoil experiment as a benchmark for broadband noise modeling," *Theoretical and Computational Fluid Dynamics*, Vol. 19, No. 3, 2005, pp. 171–196. https://doi.org/10.1007/s00162-004-0108-6.

[41] Lorenzoni, V., Tuinstra, M., and Scarano, F., "On the use of time-resolved particle image velocimetry for the investigation of rod–airfoil aeroacoustics," *Journal of Sound and Vibration*, Vol. 331, No. 23, 2012, pp. 5012–5027. https://doi.org/10.1016/j.jsv.2012.05.034.

[42] Batten, P., Goldberg, U., and Chakravarthy, S., "Interfacing Statistical Turbulence Closures with Large-Eddy Simulation," *AIAA Journal*, Vol. 42, No. 3, 2004, pp. 485–492. https://doi.org/10.2514/1.3496.

[43] Bogey, C., and Bailly, C., "Effects of Inflow Conditions and Forcing on Subsonic Jet Flows and Noise," *AIAA journal*, Vol. 43, No. 5, 2005, pp. 1000–1007. https://doi.org/10.2514/1.7465.

[44] Satcunathan, S., Zamponi, R., Meinke, M., Van de Wyer, N., Schram, C., and Schröder, W., "Validation of a model for acoustic absorption in porous media," *48th International Congress and Exhibition on Noise Control Engineering*, Institute of Noise Control Engineering, Madrid, Spain, 2019, pp. 4329–4344.

[45] Welch, P., "The use of fast Fourier transform for the estimation of power spectra: A method based on time averaging over short, modified periodograms," *IEEE Transactions on Audio and Electroacoustics*, Vol. 15, No. 2, 1967, pp. 70–73. https://doi.org/10.1109/TAU.1967.1161901.

[46] Graftieaux, L., Michard, M., and Grosjean, N., "Combining PIV, POD and vortex identification algorithms for the study of unsteady turbulent swirling flows," *Measurement Science and Technology*, Vol. 12, No. 9, 2001, pp. 1422–1429. https://doi.org/10/b47bt3.

[47] Breugem, W., "The influence of wall permeability on laminar and turbulent flows: Theory and simulations," Ph.D. thesis, Delft University of Technology, Jan. 2005.

[48] Amiet, R. K., "Acoustic radiation from an airfoil in a turbulent stream," *Journal of Sound and Vibration*, Vol. 41, No. 4, 1975, pp. 407–420. https://doi.org/10.1016/S0022-460X(75)80105-2.

[49] Kim, J. W., Haeri, S., and Joseph, P. F., "On the reduction of aerofoil–turbulence interaction noise associated with wavy leading edges," *Journal of Fluid Mechanics*, Vol. 792, 2016, pp. 526–552. https://doi.org/10/f8cqhd.

[50] Panton, R. L., and Linebarger, J. H., "Wall pressure spectra calculations for equilibrium boundary layers," *Journal of Fluid Mechanics*, Vol. 65, No. 2, 1974, pp. 261–287. https://doi.org/10.1017/S0022112074001388.